University of Sussex

Star Formation in the Local Environments of High-Redshift Ultraluminous Infrared Galaxies

Elizabeth Naomi Dubois

Submitted for the degree of Master of Philosophy

University of Sussex

May 2013

Declaration

I hereby declare that this thesis has not been and will not be submitted in whole or in part to another University for the award of any other degree.

Signature:

Elizabeth Naomi Dubois

UNIVERSITY OF SUSSEX

ELIZABETH NAOMI DUBOIS, MASTER OF PHILOSOPHY

STAR FORMATION IN THE LOCAL ENVIRONMENTS OF HIGH-REDSHIFT ULTRALUMINOUS INFRARED GALAXIES

SUMMARY

We present an analysis of the megaparsec scale environments of a sample of ultraluminous infrared galaxies (ULIRGs) at redshift 1.7, using far-infrared data from the Herschel Space Telescope. We compare their environments to those of a sample of fainter sources in the far-infrared which have comparable redshifts, in order to determine whether the environments of the ULIRGs host a net overdensity of star formation in comparison to that of galaxies in the field.

An overdensity could indicate the presence of possible companions forming in the vicinity of the ULIRGs, which may imply that these objects reside in protocluster environments. We search for evidence for an excess of far-infrared flux on megaparsec scales around the ULIRGs compared to the field, where the excess is modelled by a power law. This excess flux is then converted to a star formation rate density in solar masses per year per cubic megaparsec.

The presence of excess infrared flux around these objects is detected, indicating that there is an overdensity of star formation in their local environments which may be arising from obscured objects in the vicinity.

Acknowledgements

I am sincerely grateful for the infinite patience of my advisors, Dr. Seb Oliver and Dr. Duncan Farrah. It is a great pleasure to thank them for all of their guidance and help throughout this work.

Additionally, I would like to thank my examiners, Dr. Kathy Romer and Dr. David Clements, for their time and very helpful comments on my thesis.

I would like to extend my heartfelt thanks to my parents, without whose unwavering support this would not have been possible; and to my brother, for his constant encouragement.

I am also grateful for the support I received from a studentship from the South East Physics Network.

It has been a privilege to have had the opportunity to work alongside the members of the Astronomy Centre at Sussex.

Contents

List of Tables vii

List of Figures ix

1 Introduction 1

1.1 The Nature of Galaxies . . . 1

1.1.1 Galaxy Classification . . . 1

1.1.2 Galaxy Environments . . . 2

1.2 Morphology-Environment Connection . . . 3

1.2.1 Observed Dependence of Environment on Galaxy Assembly . . . 3

1.2.2 Strong and Weak Encounters Between Stars . . . 3

1.3 Infrared Astronomy . . . 4

1.4 Infrared Observatories . . . 5

1.4.1 The Infrared Space Observatory . . . 5

1.4.2 The Spitzer Space Telescope . . . 6

1.4.3 The Herschel Space Observatory . . . 6

1.5 Spectral Energy Distributions . . . 8

1.5.1 Optical Spectra . . . 8

1.5.2 Infrared Spectra . . . 8

1.5.3 Polycyclic Aromatic Hydrocarbons . . . 8

1.6 Ultraluminous Infrared Galaxies . . . 11

1.7 The Role of Environment . . . 13

2 Data 14

2.1 Data Sources . . . 14

2.1.1 The Herschel Multi-tiered Extragalactic Survey . . . 14

2.2 Sample Selection . . . 15

2.2.1 Initial Sample . . . 15

2.2.2 Extended Sample 16

3 Methodology **18**

3.1 Stacking 18

3.2 Model Selection and Fitting 20

4 Results **23**

4.1 Comparison of Model Fits 23

4.2 Star Formation in Correlated Sources 38

5 Conclusions and Future Work **40**

5.1 Conclusion 40

5.2 Future Work 41

5.2.1 Extension to all SPIRE bands and production of a stacked SED 41

5.2.2 Analysis at 24 microns 41

5.2.3 Search for bump-2 sources and their directly detected companions 41

5.2.4 Follow-up observations 41

5.2.5 Other objects 42

Bibliography **43**

A Source Lists **51**

B Source Images **54**

List of Tables

2.1 Number of samples of each type of object in each of the three fields. 17

3.1 Mean flux densities of the sources from both samples in the three different fields. 19

3.2 The effect on χ^2_{red} at 250μm from varying γ for both samples, fitted with the three-component model. 22

4.1 χ^2 and χ^2_{red} values for both samples from the fitting to the 250μm stacks for the one-, two- and three-component models. 24

4.2 Source, background and correlated flux values (in Jy/beam) from the fitting to the 250μm stacks for the one-, two- and three-component models. 25

4.3 Flux densities, FIR luminosities and star formation rates of the correlated sources at 250μm. 39

A.1 Positions, IRAC flux densities and MIPS 24μm flux densities for the first hundred ULIRGs in the Lockman-IRAC field sample. 53

List of Figures

1.1 The Hubble 'tuning fork' diagram. 2
1.2 Atmospheric transmittance as a function of wavelength of electromagnetic waves through the atmosphere. 5
1.3 Optical spectra of the elliptical galaxy NGC 4648 and the spiral galaxy NGC 1832. 8
1.4 Infrared template spectrum of an E5 elliptical galaxy and an Sb spiral galaxy. From Polletta et al., 2007. 9
1.5 SEDs of a sample of galaxies from Smith et al (2007) showing the PAH features. 10
1.6 Evolution of the comoving IR energy density up to z = 1 and the respective contributions from low-luminosity galaxies, IR-luminous sources and ULIRGs. . . . 12

3.1 Stacked 2D images of the bump ULIRG and comparison sample sources at 250 μm in the three different fields. 19
3.2 Models of the point spread function and correlation function. 21
3.3 Variation of χ^2_{red} with the correlation function power gamma. 21

4.1 1D radial profiles of the stacked sources for both samples in CDFS, with a model containing the source PSF only. 26
4.2 1D radial profiles of the stacked sources for both samples in EN1, with a model containing the source PSF only. 27
4.3 1D radial profiles of the stacked sources for both samples in LS, with a model containing the source PSF only. 28
4.4 1D radial profiles of the stacked sources for both samples in CDFS, with a model containing the source PSF plus a constant background. 29
4.5 1D radial profiles of the stacked sources for both samples in EN1, with a model containing the source PSF plus a constant background. 30
4.6 1D radial profiles of the stacked sources for both samples in LS, with a model containing the source PSF plus a constant background. 31

4.7 1D radial profiles of the stacked sources for both samples in CDFS, with a model containing the source PSF plus a correlation function. 32
4.8 1D radial profiles of the stacked sources for both samples in EN1, with a model containing the source PSF plus a correlation function. 33
4.9 1D radial profiles of the stacked sources for both samples in LS, with a model containing the source PSF plus a correlation function. 34
4.10 1D radial profiles of the stacked sources for both samples in CDFS, with a model containing the source PSF, a correlation function and a constant background. . . . 35
4.11 1D radial profiles of the stacked sources for both samples in EN1, with a model containing the source PSF, a correlation function and a constant background. . . . 36
4.12 1D radial profiles of the stacked sources for both samples in LS, with a model containing the source PSF, a correlation function and a constant background. . . . 37

B.1 Postage stamp images at IRAC and 24 μm wavelengths for the first hundred ULIRGs in the Lockman-IRAC field sample. 61

Chapter 1

Introduction

1.1 The Nature of Galaxies

1.1.1 Galaxy Classification

The realisation that some of the nebulae visible in the night sky are separate systems of stars like our own Milky Way took place in the early 1920s. These galaxies were first arranged into a widely accepted classification system by Hubble (1926) who organised galaxies based on their morphologies. Galaxies are broadly classed into three main forms:

- spirals, which are disc-shaped objects with several arms extending from a central nucleus in a spiral shape;
- ellipticals, which are broadly spheroidal in shape;
- irregulars, which have no definite shape.

These morphologies were described in the 'tuning fork' framework by Hubble (1936) in his work *The Realm of the Nebulae*. This is shown in Figure 1.1.

In the Hubble tuning fork scheme, spiral galaxies are divided into two types: ordinary spirals, and those in which the arms emerge from a bar-like central structure, known as barred spirals. These are further subdivided based on the sizes of their nuclei and how tightly coiled the spiral arms are. Elliptical galaxies are categorised according to how flattened or circular their ellipse shapes are.

The Hubble classification scheme has since been modified by de Vaucouleurs (1959), van den Bergh (1960) and Elmegreen and Elmegreen (1982), who have made additions to Hubble's system. Another classification scheme was devised by Morgan (1958), in which galaxies are classified primarily based on the concentration of light in their centres.

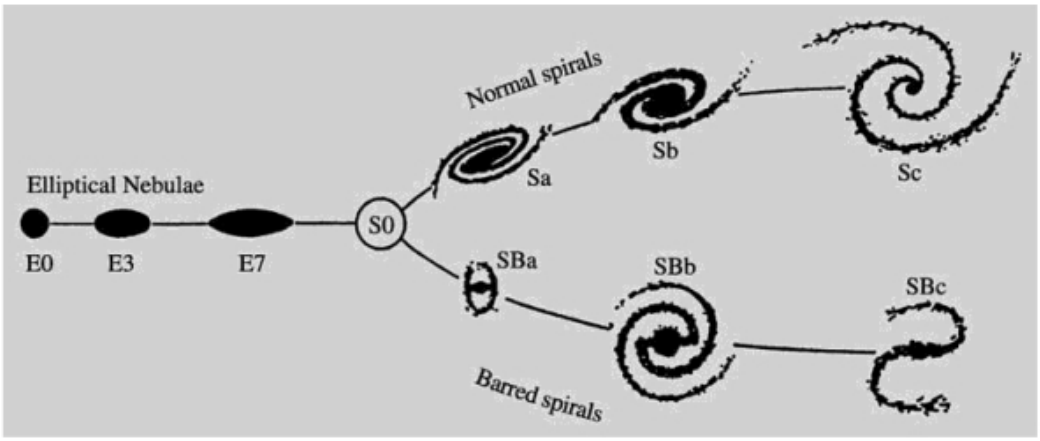

Figure 1.1: The Hubble 'tuning fork' diagram.

Classifying galaxies on the basis of their morphologies is useful because it can, to some extent, distinguish physical differences between galaxy types. The goal of studying these types is to be able to formulate an interpretation of how these objects evolve.

1.1.2 Galaxy Environments

The distribution of galaxies in space is not even, nor are these objects randomly distributed throughout the Universe. The large-scale structure of space more closely resembles a sponge, with filaments containing high densities of galaxies enclosing large regions which contain few or no galaxies, known as voids. The regions containing galaxies are categorised into three main types of environment: field, group and cluster.

Clusters The regions of space with the highest densities of galaxies are found where the filaments intersect. These contain large numbers of galaxies which are gravitationally bound into systems called galaxy clusters. These typically contain between fifty and a thousand galaxies, as well as hot intergalactic gas and dark matter.

Groups If an aggregation of galaxies consists of less than fifty members, it is known as a group. For example, the 'Local Group' contains our own galaxy, the Milky Way. These are the smallest collections of galaxies and are typically about a megaparsec in diameter. The majority of local galaxies are found in groups.

Superclusters On larger scales, galaxy clusters and groups are themselves gravitationally bound into superclusters, which are some of the largest known structures in the Universe. Our Local

Group is contained within the Virgo Supercluster.

Field If a galaxy is alone, not being gravitationally bound in a group or cluster, it is known as a field galaxy.

Voids In between these large-scale structures are immense regions containing very few or no galaxies. These vast empty voids are greater than 10 Mpc in diameter, but can be over 100 Mpc across. Particularly sparse areas are known as supervoids.

Galaxies are surrounded by a nearly spherical halo of dark matter. The size of this region is known as the virial radius, which is approximately the radius that contains an average density greater than two hundred times the critical density. A typical estimate of the virial radius of a rich cluster is approximately 1 Mpc (Saslaw, 1987). The separation between galaxy clusters is typically of the order of 10 Mpc (Deza and Deza, 2012). These scales are therefore chosen to be the intrahalo and interhalo sizes respectively in this study.

1.2 Morphology-Environment Connection

There is a relation between the type of galaxy and the environment in which it is found. In general, elliptical galaxies are found preferentially in groups or clusters (Postman and Geller, 1984), and most of the field population consist of disc/spiral galaxies. This poses the question of whether the density of the environment affects the type of galaxies that form, as well as the possibility that spirals merge to form ellipticals in dense environments.

1.2.1 Observed Dependence of Environment on Galaxy Assembly

Galaxy assembly initially took place in the higher density regions of the Universe. The first galaxies were formed fairly rapidly, in regions which had a slight overdensity in baryons. At lower redshifts, as time progressed, galaxy assembly gradually shifted out of high density regions and into the field. This occurs because once stars are made and a galaxy is assembled, the baryons in that region of the Universe become effectively collisionless. If two galaxies were composed of nothing but stars, and those two galaxies collide together, the individual stars would never collide.

1.2.2 Strong and Weak Encounters Between Stars

Stars do not individually interact with each other, for example our Sun does not interact with Proxima Centauri at all. As a star moves through the galaxy, its individual encounters are of no

significance. The implications of this are that once baryons are assembled into stars, they are no longer able to collide with each other and so it is not possible to form new stars. Once stars are formed in overdense environments early on, the amount of star formation begins to decrease. The star formation rate per comoving volume element begins to decrease, and in relative terms, more star formation begins to occur in the field.

At high redshift, star formation preferentially occurs in overdense regions, and when looking from $z = 10$ to $z = 0$, galaxy assembly shifts from primarily occuring in overdense regions to primarily happening in average density regions.

1.3 Infrared Astronomy

Astronomy is somewhat special amongst the sciences insofar as it is carried out using observations rather than experiments. Apart from samples obtained from the Moon and nearby solar system, our knowledge of the universe and all it contains has been obtained by collecting and analysing the electromagnetic radiation emitted by objects within it.

From the Earth's surface, however, it is not possible to observe all areas of the spectrum due to some wavelengths being absorbed by the atmosphere. This includes the infrared region, running from about 1 to 1000 μm. If we are to view the universe in all wavelengths, therefore, it is necessary for us to send satellites above the atmosphere to view those areas of the spectrum which cannot be observed from the ground. Figure 1.2 shows the atmospheric transmittance as a function of wavelength of electromagnetic waves through the atmosphere.

The importance of infrared astronomy is manifold. It is very useful for studying dusty regions of the universe, which are ubiquitous since many stars and galaxies are found in dusty environments. These dust grains absorbs the visible and ultraviolet light that has been emitted by nearby stars and active galactic nuclei (AGN), and re-radiates it at infrared wavelengths. This enables the observation of parts of the universe that are unable to be seen at visible wavelengths due to the dust obscuration.

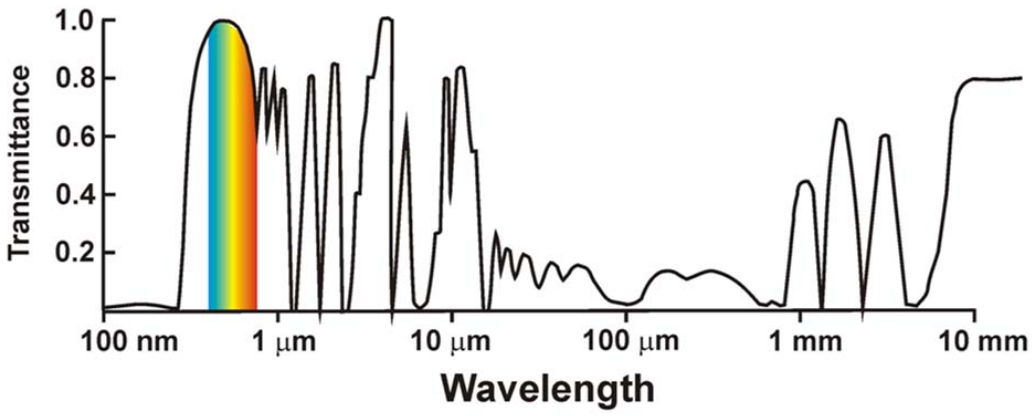

Figure 1.2: Atmospheric transmittance as a function of wavelength of electromagnetic waves through the Earth's atmosphere.
Figure from https://www.eeb.ucla.edu/test/faculty/nezlin/SatellitesAndSensors.htm.

1.4 Infrared Observatories

The first survey of the entire sky in the infrared was carried out by the Infrared Astronomical Satellite (IRAS), which operated from January to November 1983 (Neugebauer et al., 1984). It discovered about 350,000 stars and galaxies using a 60 cm telescope, 75,000 of which are galaxies which are very luminous in the infrared due to their high rates of star formation ('Introduction to IRAS', retrieved from http://irsa.ipac.caltech.edu/IRASdocs/iras.html). It is these galaxies which are investigated in this work, using data from the successors to IRAS, the Spitzer and Herschel space telescopes, which are outlined below. These observatories have enabled data to be gathered on this class of object whose main emission is at infrared wavelengths.

1.4.1 The Infrared Space Observatory

The Infrared Space Observatory (ISO) was launched by the European Space Agency (ESA) in November 1995, into a geocentric orbit. With a 60 cm primary mirror and four instruments for imaging and photometry, ISO gathered an extensive data set during the 28 months of its operation, almost a year longer than originally planned. The mission was a great success, some of the science highlights being the detection of planet formation around old stars, the discovery of large quantities of cosmic dust in intergalactic space, and finding evidence for the presence of protoplanetary disks.

1.4.2 The Spitzer Space Telescope

Initially named the Space Infrared Telescope Facility, the Spitzer Space Telescope (Werner et al., 2004), was launched in 2003 as the final mission of NASA's Great Observatories Program. Spitzer operated in its main mission, in which it was cryogenically cooled to a temperature of 5 K, until its supply of liquid helium expired in 2009. After this time it began a 'warm' mission, in which it continues to operate, using only its two shorter wavelength detectors of one instrument.

The spacecraft is comprised of the Cryogenic Telescope Assembly, which contains an 85 cm primary mirror and the following three scientific instruments, all of which were used in the cryogenic mission:

- The Infrared Array Camera (IRAC, Fazio et al. 2004), a near-infrared imager which has four detectors that operate at 3.6. 4.5, 5.8 and 8.0 μm;
- The Infrared Spectrograph (IRS, Houck et al. 2004), providing spectrometry at mid-infrared wavelengths from 5 to 40 μm;
- The Multiband Imaging Photometer (MIPS, Rieke et al. 2004), an array of three mid- to far-infrared imaging detectors which operate at 24, 70 and 160 μm.

In this work, Spitzer data from the IRAC and MIPS cameras are utilised to study the environs of the ULIRG samples in the near- and mid-infrared. This data is taken from the Spitzer Wide-area Infra Red Extragalactic survey (SWIRE, Lonsdale et al. 2003), which was one of the largest programs undertaken by the Spitzer observatory during its first year, in which over two million galaxies were imaged in six different survey fields over an area of fifty square degrees on the sky.

1.4.3 The Herschel Space Observatory

Launched on 14 May 2009 - the day before Spitzer's helium supply was exhausted - the Herschel Space Observatory (Pilbratt, G. L. et al. (2010), formerly the Far Infrared and Sub-millimetre Telescope), is the largest space-based infrared telescope. Herschel was launched jointly with the Planck satellite (a mission to map the cosmic microwave background) on an Ariane 5 launcher.

Herschel was sent into orbit around the second Lagrangian point (L2). This is a particularly stable location, 1.5 million km away from the Earth, to which many spacecraft are sent. At L2 the gravitational forces are balanced with the orbital motion of the spacecraft, and telescopes sent there do not orbit the Earth, avoiding the temperature variations that would be caused by motion through the planet's shadow.

The aims of the Herschel mission were to study how galaxies formed and evolved in the early

Universe, as well as the formation and evolution of stars and how these interact with the interstellar medium.

Operating between 60 to 670 μm, Herschel is sensitive to the coolest objects in the universe, such as dusty star-forming galaxies. It is equipped with a 3.5 m primary mirror and, like Spitzer, its science payload also consists of three instruments:

- The Heterodyne Instrument for the Far Infrared (HIFI, de Graauw et al. 2010), a spectrometer with very high resolution that can image in two wavebands simultaneously;

- The Photodetecting Array Camera and Spectrometer (PACS, Poglitsch et al. 2010), a medium resolution grating spectrometer and imaging photometer;

- The Spectral and Photometric Imaging Receiver (SPIRE, Griffin et al. 2010), a lower resolution spectrometer and imaging camera centred at 250, 350 and 500 μm.

The Herschel data used in this project is taken from the SPIRE instrument, primarily at 250 μm.

HIFI This spectrometer provided comprehensive coverage of the far-infrared and submillimeter spectrum in six bands. These cover the two regions of frequencies from 480 to 1250 GHz, and from 1410 to1910 GHz. A heterodyne instrument is a type of spectrometer that uses a technique which changes the frequency of the incoming photons to a lower frequency, resulting in an improvement in resolution.

PACS This instrument is made of of two components. Its imaging camera has the ability to observe in two bands simultaneously, covering the wavelength ranges 60-85 μm or 85-130 μm and 130-210 μm. These ranges were chosen because the radiation emitted from interstellar dust is redshifted into these wavelengths. The reflection grating spectrometer covers a similar range, from 55 to 210 μm.

SPIRE Herschel's SPIRE instrument consists of a three-band imaging photometer and a Fourier transform spectrometer. The latter is an instrument that uses a measurement technique by which the coherence of a source is used to obtain a spectrum. The technique involves the use of a Michelson interferometer, which is a moveable mirror which can be used to produce an interference pattern that is the Fourier transform of the spectrum of the source.

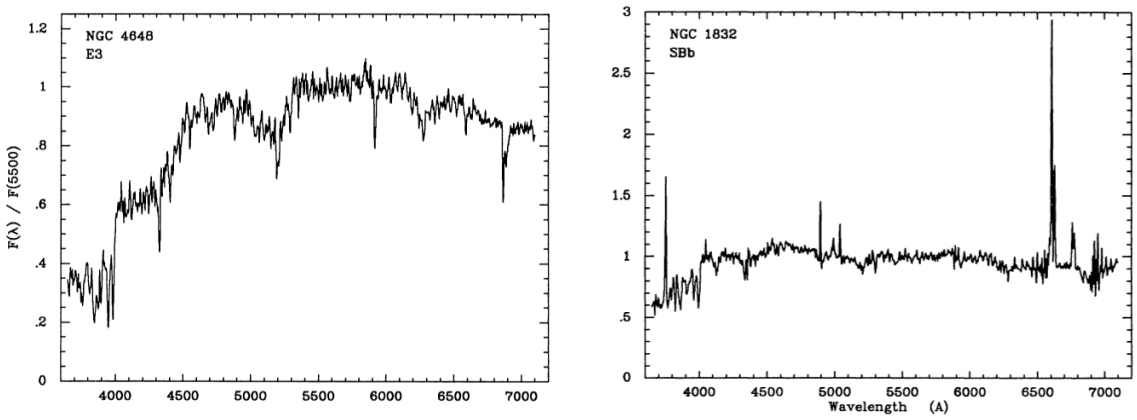

Figure 1.3: Optical spectra of the elliptical galaxy NGC 4648 (left) and the spiral galaxy NGC 1832 (right).

1.5 Spectral Energy Distributions

1.5.1 Optical Spectra

Here the features of the optical spectrum of a typical galaxy are considered. Figure 1.3 shows the characteristic optical spectra of an elliptical and a spiral galaxy respectively, from Kennicutt (1992).

The spectral energy distributions of elliptical galaxies are primarily characterised by strong absorption lines. These are caused by metals present in the atmospheres of these stars, which in elliptical galaxies are an old population. The lack of emission lines is due to the sparsity of young stars and gas in these galaxies.

Spiral galaxy spectra are, in contrast, dominated by strong emission lines, caused by their gas being heated by the young, hot stellar population. Some absorption features are also present from older, cooler stars. Strong emission lines also feature in the spectra of irregular galaxies.

1.5.2 Infrared Spectra

Similarly, the spectral energy distributions of elliptical and spiral galaxies can be compared in the infrared part of the spectrum. Figure 1.4 shows an template spectrum of each of these from the SWIRE template library (Polletta et al., 2007).

1.5.3 Polycyclic Aromatic Hydrocarbons

Star-forming galaxies display strong emission features due to the presence of organic compounds consisting of large molecules called polycyclic aromatic hydrocarbons (PAHs). The brighter PAH

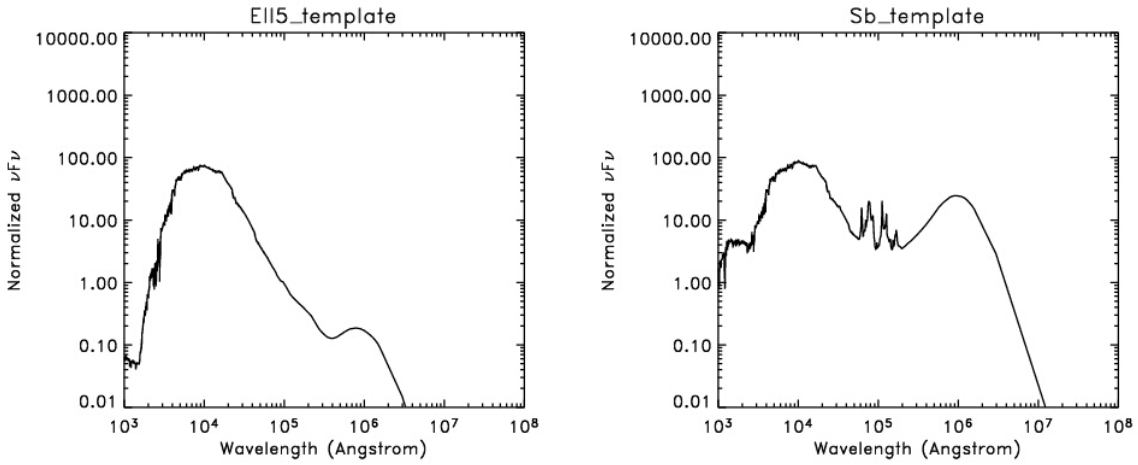

Figure 1.4: Infrared template spectrum of an E5 elliptical galaxy and an Sb spiral galaxy. From Polletta et al., 2007.

spectral bands are found at 6.2, 7.7, 8.6, 11.3 and 12.7 μm. PAHs do not originate from the stars themselves, but from a transition zone between the material that the star is ionising and the neutral material of the general interstellar medium. This region is known as the photodissociation region, and is where PAHs are thought to arise.

It is expected for PAHs to be very prominent in star-forming galaxies, because they arise from photodissociation regions around newly-formed stars; in quiescent galaxies they are weaker. Figure 1.5 shows the PAHs in a sample of galaxies from Smith (2007).

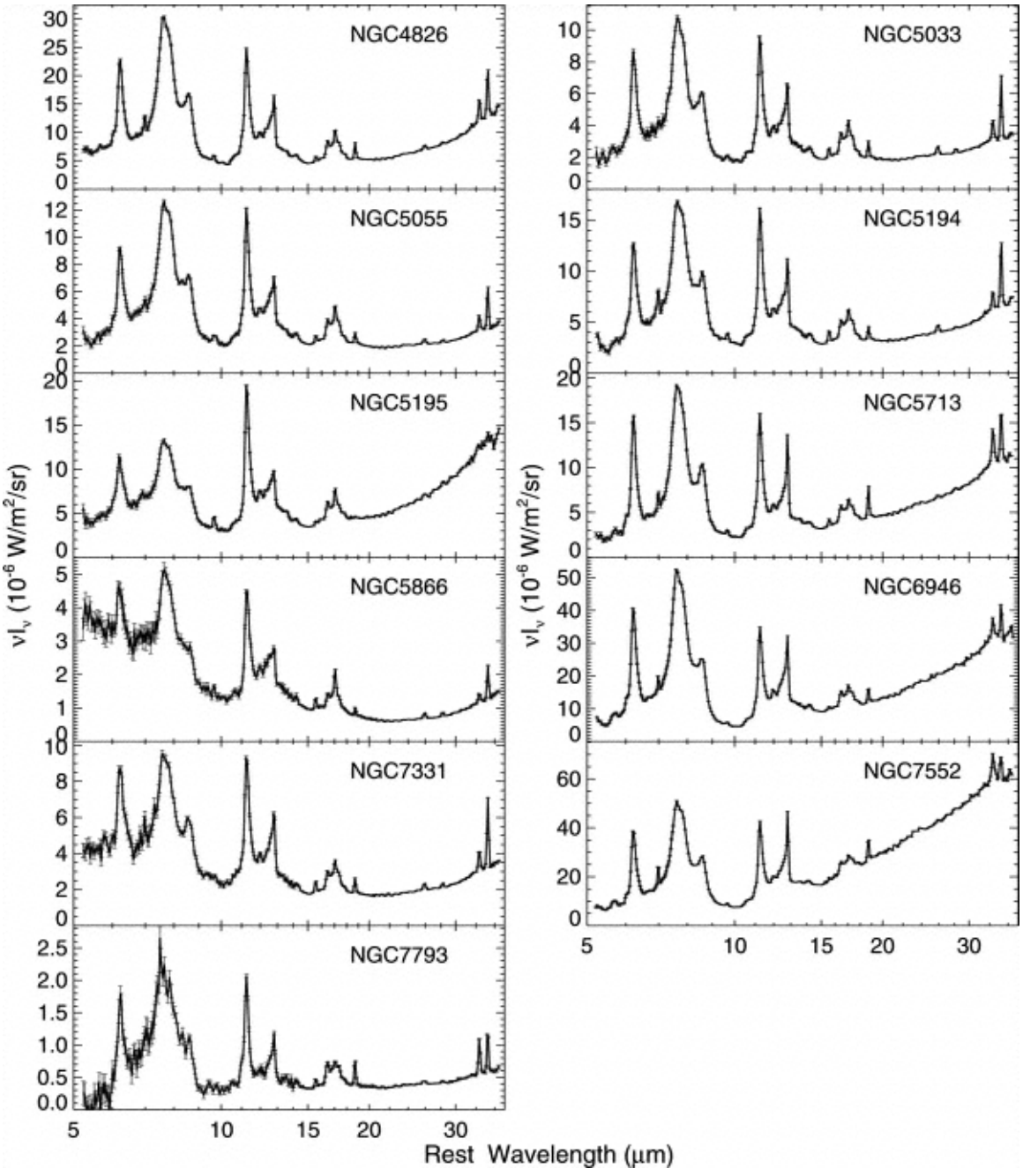

Figure 1.5: SEDs of a sample of galaxies from Smith et al (2007) showing the PAH features.

1.6 Ultraluminous Infrared Galaxies

A population of galaxies showing unusually high infrared emission was first discovered in the 1970s using ground-based photometry (Rieke and Low, 1972). These objects were subsequently detected in much larger numbers by the IRAS satellite in the 1980s (Soifer et al., 1984; Rowan-Robinson et al., 1984). Such galaxies, having luminosities greater than $10^{11} L_{\odot}$ are known as luminous infrared galaxies (LIRGs). Those that are even brighter, with L $> 10^{12} L_{\odot}$ are called ultraluminous infrared galaxies (ULIRGs), and the most extreme of these, with L $> 10^{13} L_{\odot}$, are the hyperluminous infrared galaxies (HLIRGs).

These objects are rare in the local universe, comprising only 3% of galaxies (Soifer et al., 1987), but far more numerous at high redshift (Le Floc'h, E. et al., 2005); a plot from this paper showing the variation with redshift of LIRGs, ULIRGs and low luminosity galaxies is shown in Figure 1.6.The black points with the vertical and horizontal lines represent the integrated star formation rate densities and their uncertainties. These have been estimated within various redshift bins, and are taken from the literature. At $z > 2$, these objects comprise the majority of the infrared background and account for most of the star formation activity (e.g. Blain et al. (2002). For a detailed review see Sanders and Mirabel (1996) and Lonsdale (2006)).

Much has been learned about these galaxies from detailed studies in all areas of the spectrum, including the nature of the power source fuelling the high infrared emission from ULIRGs. Far-infrared emission can be produced by the processes of both star formation and AGN activity. In ULIRGs, this emission is thought to consist of a mixture of starburst and AGN activity, with the starburst dominating in the majority of cases. This consensus has been reached from a multi-wavelength approach, with evidence from X-ray observations (Ptak et al., 2003; Franceschini et al., 2003), optical spectroscopy (Kim et al., 1998), infrared photometry (Farrah et al., 2003), infrared spectroscopy (Armus et al., 2007; Farrah et al., 2007), and radio observations (Condon, 1992).

X-ray observations are useful in discriminating between activity from starbursts and that of AGN (Rieke, 1988). Evidence in the X-ray for ULIRGs having an AGN component has come from the detection of their characteristic power law spectra at these wavelengths. Evidence for a starburst-like component has come from optical spectroscopic surveys, which have detected the spectral signatures of young massive stars. There are also diagnostic lines in the mid-infrared region which can be used for characterising the power source of these objects.

The fraction of ULIRGs that are powered by AGN increases with luminosity: at $L < 2 \times 10^{12} L_{\odot}$ about 15% of ULIRGs are predominantly AGN powered, whereas at higher luminosities the fraction of AGN dominated ones increases to about 50% (Lagache et al., 2005), but see also

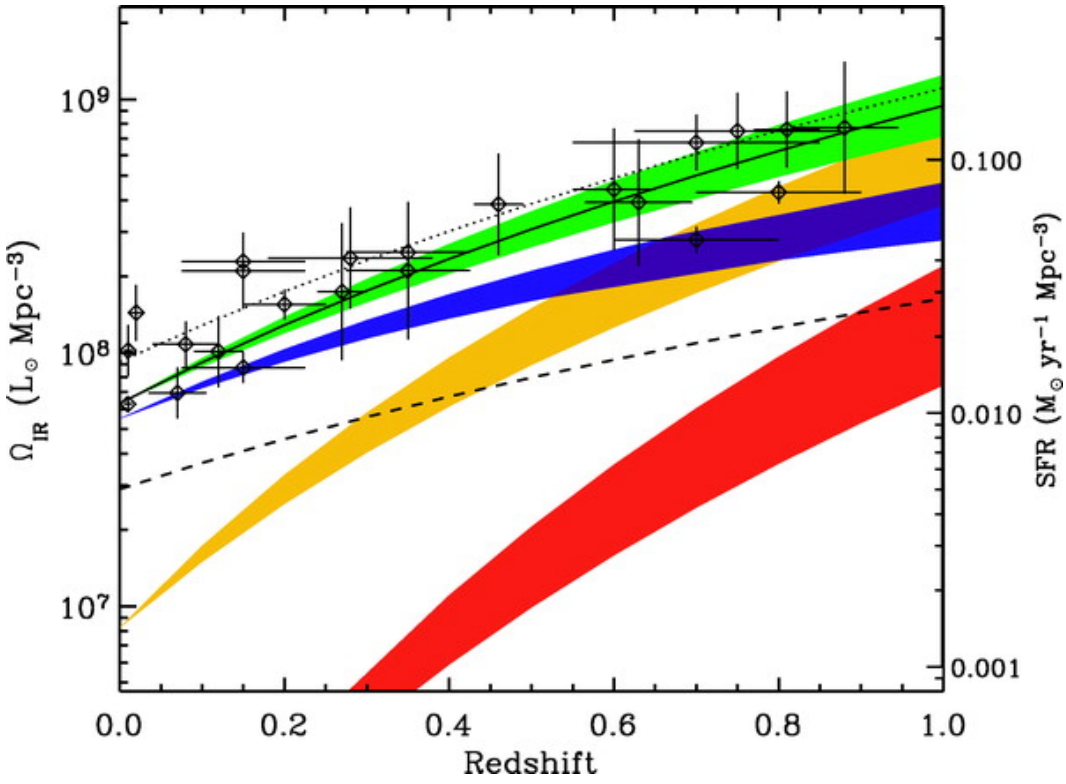

Figure 1.6: Evolution of the comoving IR energy density up to z = 1 (green) and the respective contributions from low-luminosity galaxies (blue filled), IR-luminous sources (orange), and ULIRGs (red). Figure from Le Floc'h et al (2005).

Rigopoulou et al. (1996, 1998). These objects are therefore important in understanding the history of star formation at $z > 1$.

1.7 The Role of Environment

ULIRGs are preferentially found in overdense environments at $0.7 < z < 1.0$ when compared to other galaxies at similar redshifts (Marcillac et al., 2008), with possible companions often being observed in their vicinities. If it is the case that ULIRGs are the progenitors of local massive elliptical galaxies, they would reside in overdense regions at high redshift (Blain et al., 2004). This overdensity is in galaxies, but here we investigate whether it also holds for star formation rate density. An opportunity then arises to gain an insight into massive galaxy assembly by studying the environments of these objects. One approach to this is to ascertain whether the environments of the ULIRGs - as well as the ULIRG itself - have a greater rate of star formation compared to that of galaxies in the field. This could be achieved by studying intrahalo ULIRG environments at high redshift, and comparing these environments to those of more quiescent galaxies at similar redshifts.

Intrahalo environments are those on small scales, within a dark matter halo, on scales of about $\sim$1 h^{-1} Mpc, the size of a typical halo. Interhalo environments are on larger scales of $\sim$10 h^{-1} Mpc. In this work we are investigating local environments, so those corresponding to a region of about 1 Mpc radius around the central source. This is in order to determine whether there are obscured sources associated with the ULIRG that reside within its halo. This is done by undertaking a search on these scales for overdensities of sub-mm flux around two samples of high-redshift ULIRGs. A detection of such an excess may indicate the formation of their cluster companions. Indications that this may be the case have arisen from models for enhanced star formation rate densities in overdense regions at high redshift, e.g. Hopkins et al. (2010).

The data and sample selection is described in Chapter 2, and the methodology is explained in Chapter 3. Results are presented in Chapter 4. Finally, a discussion and summary of the main conclusions is given in Chapter 5 on page 40. Throughout this thesis we assume a flat cosmology of $\Lambda = 0.7$, $\Omega_0 = 0.3$ and $H_0 = 70$ km s^{-1}Mpc^{-1}.

Chapter 2

Data

2.1 Data Sources

In this chapter, the sources of data used in this work are described, along with the survey from which they were obtained and the source selection criteria which has been applied.

2.1.1 The Herschel Multi-tiered Extragalactic Survey

Herschel's largest science project is the Herschel Multi-tiered Extragalactic Survey (HerMES, Oliver et al. (2012)), whose primary aim is to study the evolution of galaxies in the distant universe. As Herschel has the ability to see light being reprocessed by the obscuring dust, it is able to observe the moments at which galaxies are undergoing their most intense phases of star formation.

The survey includes Herschel SPIRE sky maps and object catalogues, containing over 100,000 sources. The sky is surveyed using a hierarchical structure, with seven tiers ranging from small areas with deep observations of clusters, to larger areas with shallower coverage covering about 270 square degrees.

The justification for using this tiered approach in the HerMES survey is that the survey was designed to fulfil a number of objectives. These include the determination of the total far-infrared luminosity function, constraining models of star formation activity and the role of environment, and the search for rare, exotic objects and lensed systems.

There are advantages to the design of the survey comprising a number of different tiers. It enables observations which cover a range of different depths and areas. This means that a variety of different sources can be observed. The wide, shallow tiers sample brighter objects, which have high luminosities and are rare. The deep, narrow tiers sample the more common, lower luminosity galaxies, which are faint and confused. Source confusion is an issue which affects Herschel, particularly the SPIRE instrument. This is a noise factor which limits the sensitivity; below a

certain level of fluctuations of the sky brightness, called the confusion limit, sources cannot be individually detected.

This work uses data from the HerMES maps and catalogues for three fields: Lockman-SWIRE, Chandra Deep Field South (CDFS), and the European Large-Area ISO Survey (ELAIS) N1.

2.2 Sample Selection

2.2.1 Initial Sample

The sources that were initially selected for study were the 31 ULIRGs observed in Farrah et al. (2008) (not including the 32nd object that is not in the Lockman field). These galaxies are appropriate for this study since they have high rates of star formation and are all in a narrow redshift range. The choice of these objects was based on a number of factors:

- The PAH features in their spectra indicate that their infrared emission is dominated by starbursts rather than AGN;
- They are at redshift 1.7, which lies within the epoch at which the peak of star forming activity occurred;
- They have spectroscopic redshifts;
- They have high 24 μm luminosities, indicating significant star forming activity;
- Their spectra show the presence of an apparent broad emission feature at 1.6 μm.

Objects exhibiting the spectral feature mentioned in the latter point are known as 'bump-selected' galaxies or 'IRAC-peakers', if the bump is redshifted into one of the four IRAC bands, in which case they are numbered by which band it is redshifted into. The four IRAC bands are 3.6, 4.5, 5.8 and 8.0 μm. The 31 sources used here are bump-2 objects, meaning that they have a higher flux in the second IRAC band, 4.5 μm, than in the other three: $f_{3.6} < f_{4.5}$, $f_{4.5} > f_{5.8}$ and $f_{4.5} > f_{8.0}$.

This bump feature is produced as a result of the minimum in the opacity of H- ions in the atmospheres of late-type stars. Therefore if a galaxy spectrum shows this feature, it will harbour a significant number of evolved stars. In addition, the presence of this bump signifies that the galaxy cannot have a significant AGN continuum, since in the presence of this the bump feature would be unobservable.

The data available for the initial bump-2 selection from Farrah et al. (2008) originated from observations made with the Infrared Spectrograph (IRS) on Spitzer. Each target was centred in

the slit and observed for eight cycles, each of 120 seconds duration. The data were subsequently reduced and cleaned by processing through the pipeline reduction software of the Spitzer Science Centre. This carried out the processes of dark current subraction, bad pixel removal and sky subtraction.

The sources in this sample have spectroscopic redshift confirmation, because all of the these objects have IRS spectra. The majority of these (all but three) have a reliable redshift that has been obtained from this IRS spectra.

2.2.2 Extended Sample

The process used to expand the bump-2 selection to a broader Herschel sample is as follows. A larger sample then gathered in order to garner a better understanding of their environments by looking at a larger sample of objects. This was obtained by searching in other areas of the sky as well as in the Lockman-SWIRE region. Two additional HerMES fields were chosen for the search: CDFS and ELAIS N1. A total of 646 sources were found in Lockman-SWIRE, 490 in ELAIS N1 and 486 in CDFS, giving a total of 1622 bump ULIRGs. A check was performed to confirm that the number of sources found in each field was statistically consistent. The number found per square degree in each field was determined to be consistent within the Poisson errors of the mean number of sources per square degree.

A selection of actively starforming galaxies, with a substantial mass of evolved stars already in place, can be obtained by combining the bump selection with a high infrared luminosity, and selecting those objects with a bright 24 μm flux. A value of 350 μJy was chosen for the 24 μm flux cut, as a high value of 24μm emission should correspond to objects with a high rate of star formation. The comparison sample was chosen to have 24 μm fluxes of less than 350 μJy, the opposite criteria to the initial sample, in order that none of the objects can appear in both. The numbers of these sources found were 2825 in Lockman-SWIRE, 2328 in EN1 and 2436 in CDFS, giving a total of 7589 bump sources which have a smaller 24 μm flux than in the initial sample. This is summarised in Table 2.2.2.

Clearly from this table, there has been a marked increase in the number of sources from the initial 31 which were the starting sample from Farrah et al. (2008). This has been expanded to find all sources which satisfy the general selection criteria, and extended to a wider area of the sky, which resulted in the large increase in sample size.

The data is thus split into two samples, each of which containing three subsamples from the three different fields. The flux cut for the comparison sample will preferentially select bump sources which are not undergoing a starburst phase. This is a result of the 24 μm bright objects

	Number of objects		
	CDFS	EN1	LS
24 μm flux $>$ 350 μJy	486	490	646
24 μm flux $<$ 350 μJy	2436	2328	2825

Table 2.1: Number of samples of each type of object in each of the three fields.

featuring the rest frame 7.7 μm polycyclic aromatic hydrocarbon lines in their spectra, which have been redshifted to 24 μm. These are an indicator of star formation activity, so this approach should therefore reveal any difference in environment between our original sample and objects which are at the same redshift, and have the same stellar mass, but have less active star formation taking place.

The only difference between the new extended sample and the original one is that the larger sample has a lower cut on the 24μm flux, in order to expand the number of sources. The value of the flux cut was chosen because at a flux of 350μJy, it can still be safely assumed that the sources are star-forming, an that the object is a starburst galaxy. 350μJy at redshift 1.7 at 24μm corresponds to a total infrared luminosity of over $10^{11} L_{\odot}$, and therefore it is has a high likelihood of being a star-forming galaxy.

The reason for splitting the samples using this particular flux cut is that although 350μJy is almost certainly still star-forming, given the luminosity that it corresponds to, objects with flux densities much below 350μJy have a greater chance of not being star forming. Hence we (semi-arbitrarily) choose 350μJy as a boundary. An alternative approach would be to say that fluxes of $>$ 350μJy are star-forming but leave a gap between the samples and say that $<$ 300 μJy, for example, is not star-forming. This approach would also be valid, but as there was no indication that any substantial difference would result between these approaches, the former was selected.

Chapter 3

Methodology

3.1 Stacking

Postage stamp images of all of the sources were taken from the Herschel SPIRE maps at 250μm. A 21 x 21 pixel region was cut out for each object, centred on its position. The SPIRE maps have a pixel size of 6", and the scale at z$\sim$1.7 is $\sim$8.5 kpc/", so this allows us sufficient area to sample the environments of both types of sources out to a radius of approximately 1 Mpc. This region size was chosen as being a typical size of a dark matter halo, and so should provide a sufficient sample of the interhalo environments.

A two-dimensional stack was taken of a 1 Mpc radius around the objects by summing the images in each of the three fields, in order to show the companion sources that are too faint to detect in the individual images. None of these sources were found to be directly detected by Herschel. Stacking the images gives the mean properties of the population. These stacks are shown in Figure 3.1 for both the original sample and the 24μm faint sample, and a summary of their mean properties are given in Table 3.1. The errors were found by calculating the mean error in quadrature from the fluxes.

The stacking was performed using the library codes by Béthermin, M. et al. (2010) and Bavouzet (2009). This performs the stacking of a catalogue of sources by inputting the map image and the coordinates of the sources to stack, then the mean of the stack is calculated. These two-dimensional stacked images were then converted into a one-dimensional radial profile by plotting flux against distance from the centre of the image. In this procedure the image and catalogue files are read in, and the separation between each pixel and the source is calculated. The flux is summed up in bins as a function of separation. There were several flux values for each separation, so the mean flux at each radius value was calculated, and the errors on these values were found from the standard deviation.

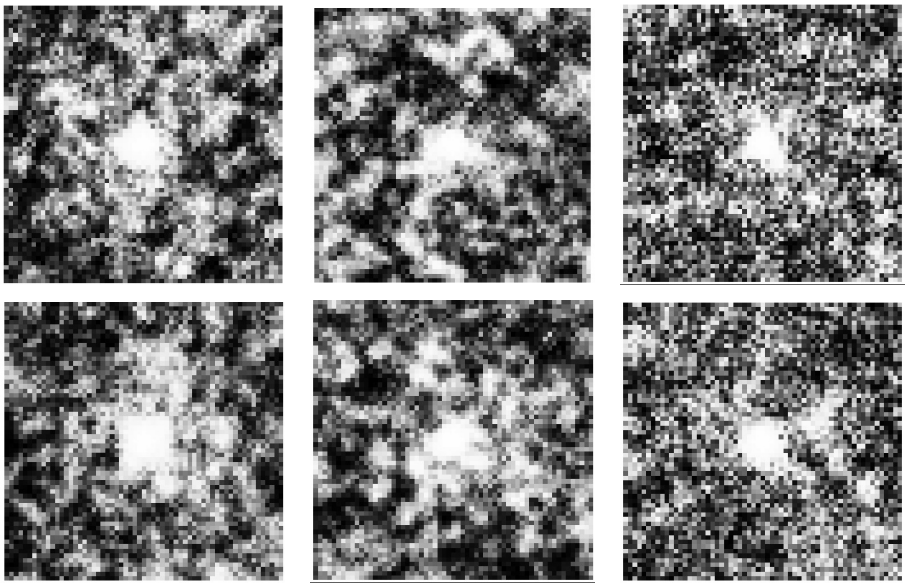

Figure 3.1: Stacked 2D images of the bump ULIRG (top) and comparison sample (bottom) sources in CDFS (left), EN1 (middle) and Lockman-SWIRE (right), at 250 μm. The image dimensions are 2 $\times$ 2 arcmin^2 and each image is 21 x 21 pixels. The pixel sizes are equal, but the noise levels are different because these sources may lie where there is lower than average coverage on the map.

		Mean 3.6μm flux (μJy)	Mean 4.5μm flux (μJy)	Mean 5.8μm flux (μJy)	Mean 8.0μm flux (μJy)	Mean 24μm flux (mJy)
24μm flux	CDFS	60.01 $\pm$ 3.60	70.39 $\pm$ 4.22	49.73 $\pm$ 2.98	54.34 $\pm$ 3.26	484.73 $\pm$ 29.1
$>$ 350 μJy	EN1	63.95 $\pm$ 3.84	73.76 $\pm$ 4.43	54.78 $\pm$ 3.29	56.41 $\pm$ 3.38	478.74 $\pm$ 28.72
	LS	62.01 $\pm$ 3.72	73.95 $\pm$ 4.44	48.45 $\pm$ 2.91	56.98 $\pm$ 3.42	485.79 $\pm$ 2.91
24μm flux	CDFS	42.66 $\pm$ 2.56	48.38 $\pm$ 2.90	38.39 $\pm$ 2.30	41.74 $\pm$ 2.50	135.08 $\pm$ 8.10
$<$ 350 μJy	EN1	44.63 $\pm$ 2.68	50.69 $\pm$ 3.04	40.89 $\pm$ 2.45	44.65 $\pm$ 2.68	136.85 $\pm$ 8.21
	LS	50.85 $\pm$ 3.05	55.85 $\pm$ 3.35	44.19 $\pm$ 2.65	44.76 $\pm$ 2.69	117.77 $\pm$ 7.07

Table 3.1: Mean flux densities of the sources from both samples in the three different fields.

3.2 Model Selection and Fitting

In order to test for the presence of obscured star formation from local objects, three model components are fit to the radial profiles: the background flux, the flux of the mean source, and that of the sources correlated with them. The model for the central source flux is obtained from the Herschel point spread function (PSF, HERSCHEL-DOC-0798 (2011)), and the background is modelled as a constant. The Herschel maps have a mean of zero so the background is expected to be close to this value. If the observed data is $d(r)$, the background b, correlated flux c and source flux f, then it can be modelled as

$$d(r) = b + f \times PSF(r) + c \times cor(r) \tag{3.1}$$

which is a linear fit of the form $z = A + Bx + Cy$, where x represents the PSF, y represents the correlation function and z is the data; then A is the background and B is the flux. The correlation function, w_θ, is related to $cor(r)$ via a convolution with the point spread function and a one-dimensional projection.

The correlation function is modelled by a power law given by $w_\theta = d^\gamma$, where d is the distance to the centre of the image, and the power γ is a constant. This constant is varied in order to find the uncertainty introduced by an unknown value. We begin by using an initial value of γ = -0.7, as this has been found to be the best fit power law to the angular correlation function of galaxies (Maller et al., 2005). This value was incremented in both the positive and negative directions using intervals of 0.4, and the value of χ^2_{red} recorded. The results are shown in Table 3.2 and are plotted in Figure 3.3, which show that there was little variation in this parameter, and so it was not able to be constrained in the fitting process. We have therefore fixed γ at the initial value of -0.7 throughout.

Plots of the model point spread function and correlation function fit to the radial profiles of the CDFS ULIRG stack are shown in Figure 3.2.

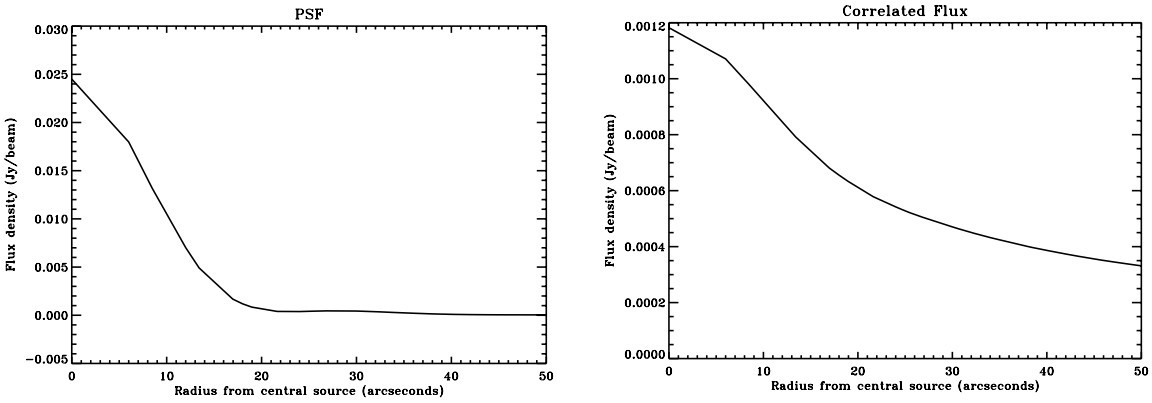

Figure 3.2: Models of the point spread function and correlation function, fit to the CDFS ULIRG data.

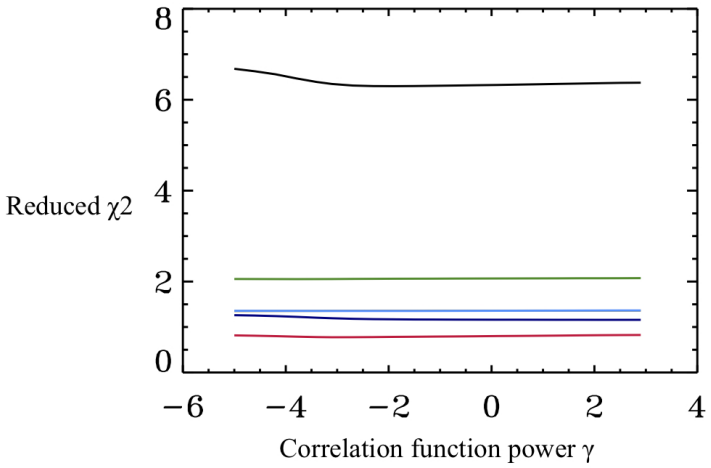

Figure 3.3: Variation of χ^2_{red} with the correlation function power γ. The dark and pale blue lines represent the comparison sample for CDFS and LS respectively; there is a third line here for EN1 that is indistinguishable from that of LS as the values differ by only up to 0.005. The red line is for the EN1 ULIRG sample; the green line represents the LS ULIRG sample; and the black line shows the CDFS ULIRG sample. The latter is significantly higher than for the other fields, the reason for which is not apparent.

γ	χ^2_{red}					
	24μm flux $>$ 350 μJy			24μm flux $<$ 350 μJy		
	CDFS	EN1	LS	CDFS	EN1	LS
+2.9	6.375	0.825	2.075	1.158	1.359	1.364
+2.5	6.371	0.823	2.074	1.158	1.359	1.364
+2.1	6.363	0.820	2.073	1.158	1.359	1.363
+1.7	6.356	0.816	2.073	1.159	1.359	1.362
+1.3	6.348	0.812	2.071	1.159	1.359	1.361
+0.9	6.340	0.808	2.070	1.160	1.360	1.360
+0.5	6.332	0.804	2.069	1.161	1.360	1.359
+0.1	6.325	0.801	2.068	1.161	1.360	1.358
-0.3	6.319	0.797	2.067	1.162	1.360	1.357
-0.7	6.312	0.793	2.066	1.163	1.360	1.356
-1.1	6.307	0.790	2.064	1.165	1.360	1.355
-1.5	6.301	0.786	2.063	1.166	1.359	1.354
-1.9	6.298	0.783	2.062	1.169	1.359	1.354
-2.3	6.300	0.779	2.060	1.173	1.359	1.354
-2.7	6.312	0.776	2.058	1.181	1.358	1.354
-3.1	6.346	0.775	2.056	1.193	1.357	1.354
-3.5	6.391	0.779	2.055	1.205	1.355	1.354
-3.9	6.470	0.788	2.054	1.224	1.354	1.355
-4.3	6.560	0.799	2.055	1.240	1.353	1.355
-4.7	6.626	0.809	2.056	1.252	1.352	1.356
-5.1	6.680	0.816	2.057	1.260	1.351	1.356

Table 3.2: The effect on χ^2_{red} at 250μm from varying γ, for the sources with 24 μm flux $>$ 350 μJy (left) and those with 24 μm flux $<$ 350 μJy (right), fitted with the three-component model.

Chapter 4

Results

4.1 Comparison of Model Fits

The amplitudes of the three model components were then computed during the fitting process using the IDL routine MPFIT. Four different models were calculated from these: the central source only, the central source plus the background, the PSF plus the correlated component, and all three components together. The values of background flux, source flux and correlated flux which were produced from the fitting were averaged for the three different fields, and the standard deviation calculated as an estimate of the uncertainties in these quantities.

In order to obtain an estimate of the accuracy of the model fits to the data, the value of χ^2 for these is calculated. Since the model fits contain different numbers of parameters, the reduced χ^2 (χ^2_{red}) is then computed in order to provide a better comparison. This is calculated using $\chi^2_{red} = \chi^2/\nu$, where ν is the number of degrees of freedom. Table 4.1 gives the χ^2 and χ^2_{red} values for both samples, and Table 4.1 shows the flux values for each component that was computed during the each of the model fits.

Figures 4.1, 4.2 and 4.3 display the flux as a function of radius for the stacked images, in each of the three fields, for both samples. The data points represent the flux density at different radii from the central source. The error bars on the data points were obtained by finding the mean and standard deviation of all the points with the same radius value. Figures 4.4, 4.5, 4.6, 4.7 and 4.8, 4.9, 4.10, 4.11 and 4.12 are repeats of the fitting shown in Figures 4.1, 4.2 and 4.3 for the other three models using only two or one component.

The figures give a visual indication of how well the various models fit the fluxes obtained from the stacked images. From this, the best fitting model can be selected, which can then be used to quantify the amount of flux that is coming from the correlated sources.

Objects	Field	Model	χ^2	χ^2_{red}
24μm flux $>$ 350 μJy	CDFS	Source Flux + Background Flux + Correlated Flux	15.24	0.53
		Source Flux + Background Flux	36.95	1.23
		Source Flux + Correlated Flux	26.41	0.88
		Source Flux	101.28	3.27
	EN1	Source Flux + Background Flux + Correlated Flux	15.35	0.53
		Source Flux + Background Flux	64.77	2.16
		Source Flux + Correlated Flux	43.08	1.44
		Source Flux	107.48	3.47
	LS	Source Flux + Background Flux + Correlated Flux	16.84	0.58
		Source Flux + Background Flux	26.46	0.88
		Source Flux + Correlated Flux	19.61	0.65
		Source Flux	64.20	2.07
24μm flux $<$ 350 μJy	CDFS	Source Flux + Background Flux + Correlated Flux	7.64	0.26
		Source Flux + Background Flux	69.30	2.31
		Source Flux + Correlated Flux	94.00	3.13
		Source Flux	126.39	4.08
	EN1	Source Flux + Background Flux + Correlated Flux	3.06	0.11
		Source Flux + Background Flux	23.72	0.79
		Source Flux + Correlated Flux	9.70	0.32
		Source Flux	104.84	3.38
	LS	Source Flux + Background Flux + Correlated Flux	6.45	0.22
		Source Flux + Background Flux	69.30	2.31
		Source Flux + Correlated Flux	52.14	1.73
		Source Flux	137.79	4.44

Table 4.1: χ^2 and χ^2_{red} values (in Jy/beam) for the sources with 24 μm flux $>$ 350 μJy (top) and those with 24 μm flux $<$ 350 μJy (bottom) from the fitting to the 250μm stacks for the one-, two- and three-component models.

Objects	Field	Model	Source Flux	Background Flux	Correlated Flux
24μm flux $>$ 350 μJy	CDFS	Source + Background + Correlated	0.02222	-0.00102	0.00406
		Source + Background	0.02539	0.00038	-
		Source + Correlated	0.00889	-	-0.00040
		Source Only	0.02620	-	-
	EN1	Source + Background + Correlated	0.02292	-0.00205	0.00700
		Source+Background	0.02759	0.00061	-
		Source+Correlated	0.02618	-	0.00191
		Source Only	0.02833	-	-
	LS	Source + Background + Correlated	0.02416	-0.00054	0.00274
		Source + Background	0.02641	0.00044	-
		Source + Correlated	0.02528	-	0.00131
		Source Only	0.02739	-	-
	μ	Source + Background + Correlated	0.02310	-0.00120	0.00460
		Source + Background	0.02646	0.00048	-
		Source + Correlated	0.02012	-	0.00094
		Source Only	0.02731	-	-
	σ	Source + Background + Correlated	0.00098	0.00077	0.00218
		Source + Background	0.00110	0.00012	-
		Source + Correlated	0.00973	-	0.00120
		Source Only	0.00107	-	-
24μm flux $<$ 350 μJy	CDFS	Source + Background + Correlated	0.00671	-0.00115	0.00255
		Source + Background	0.00868	-0.00020	-
		Source + Correlated	0.02441	-	0.00118
		Source Only	0.00832	-	-
	EN1	Source + Background + Correlated	0.00669	-0.00051	0.00234
		Source + Background	0.00837	0.00037	-
		Source + Correlated	0.00759	-	0.00104
		Source Only	0.00898	-	-
	LS	Source + Background + Correlated	0.00711	-0.00102	0.00333
		Source + Background	0.00963	0.00025	-
		Source + Correlated	0.00897	-	0.00078
		Source Only	0.01004	-	-
	μ	Source + Background + Correlated	0.00684	-0.00089	0.00274
		Source + Background	0.00889	0.00014	-
		Source + Correlated	0.01366	-	0.00100
		Source Only	0.00911	-	-
	σ	Source + Background + Correlated	0.00024	0.00034	0.00052
		Source + Background	0.00066	0.00030	-
		Source + Correlated	0.00934	-	0.00020
		Source Only	0.00087	-	-

Table 4.2: Source, background and correlated flux values (in Jy/beam) from the fitting to the 250μm stacks for the one-, two- and three-component models.

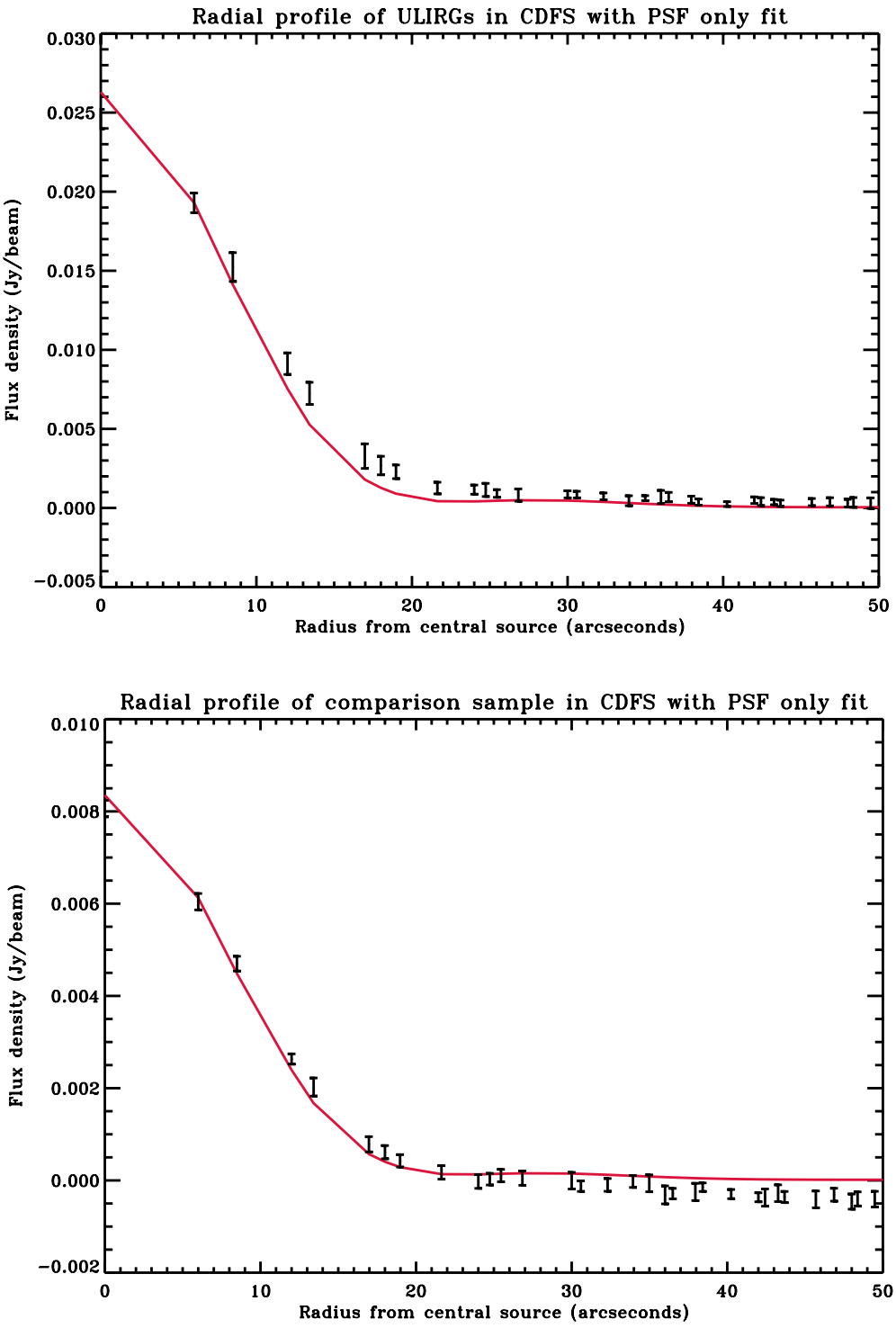

Figure 4.1: 1D radial profiles of the stacked sources for the 24μm bright (top) and 24μm faint (bottom) samples in CDFS. The data points are the flux densities at different radii from the stacked 250μm images. Error bars are calculated from the standard deviation of all points at the same radii. A model containing the PSF of the central source only (red line) is fit to the data.

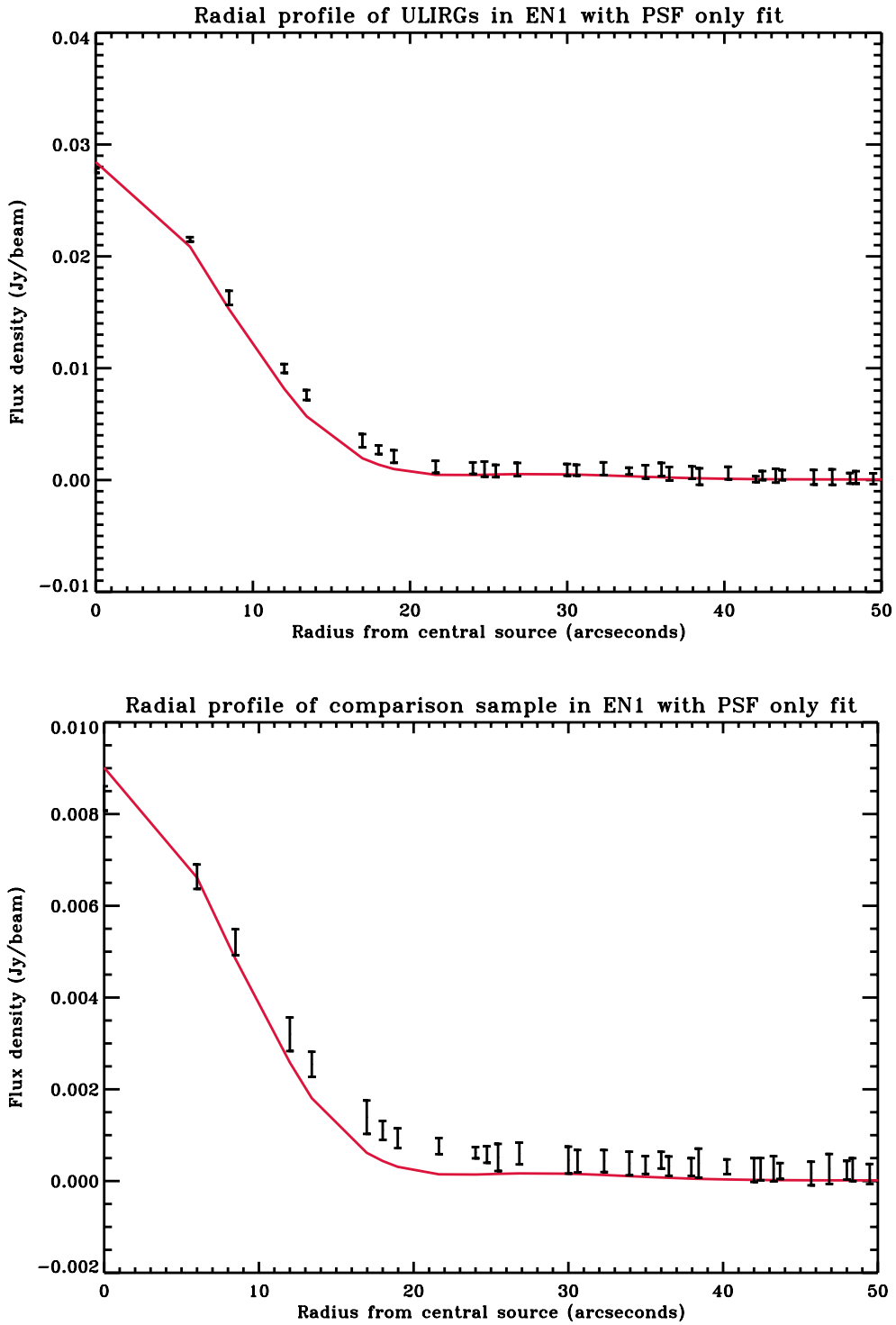

Figure 4.2: 1D radial profiles of the stacked sources for the 24μm bright (top) and 24μm faint (bottom) samples in EN1. The data points are the flux densities at different radii from the stacked 250μm images. Error bars are calculated from the standard deviation of all points at the same radii. A model containing the PSF of the central source only (red line) is fit to the data.

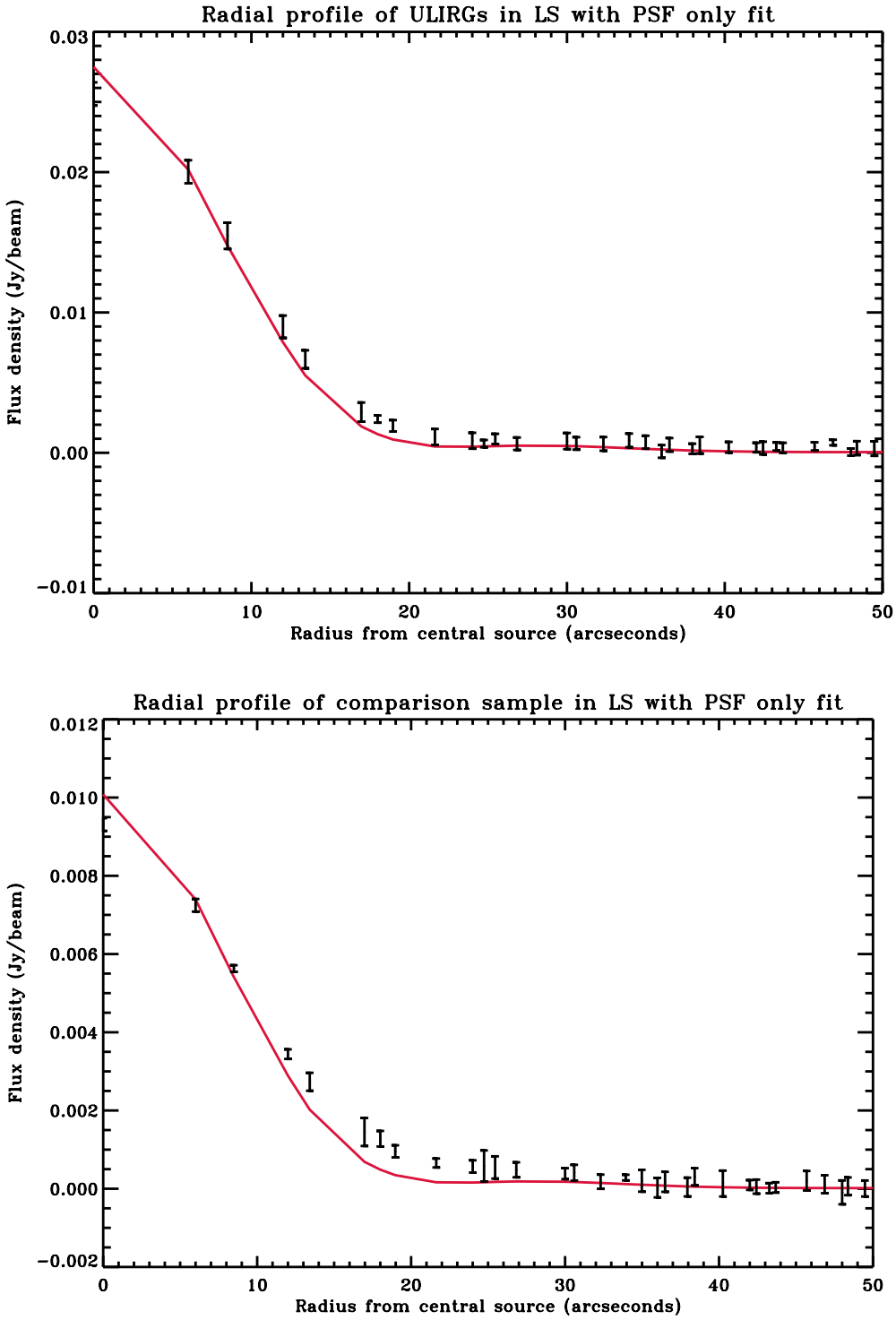

Figure 4.3: 1D radial profiles of the stacked sources for the 24μm bright (top) and 24μm faint (bottom) samples in LS. The data points are the flux densities at different radii from the stacked 250μm images. Error bars are calculated from the standard deviation of all points at the same radii. A model containing the PSF of the central source only (red line) is fit to the data.

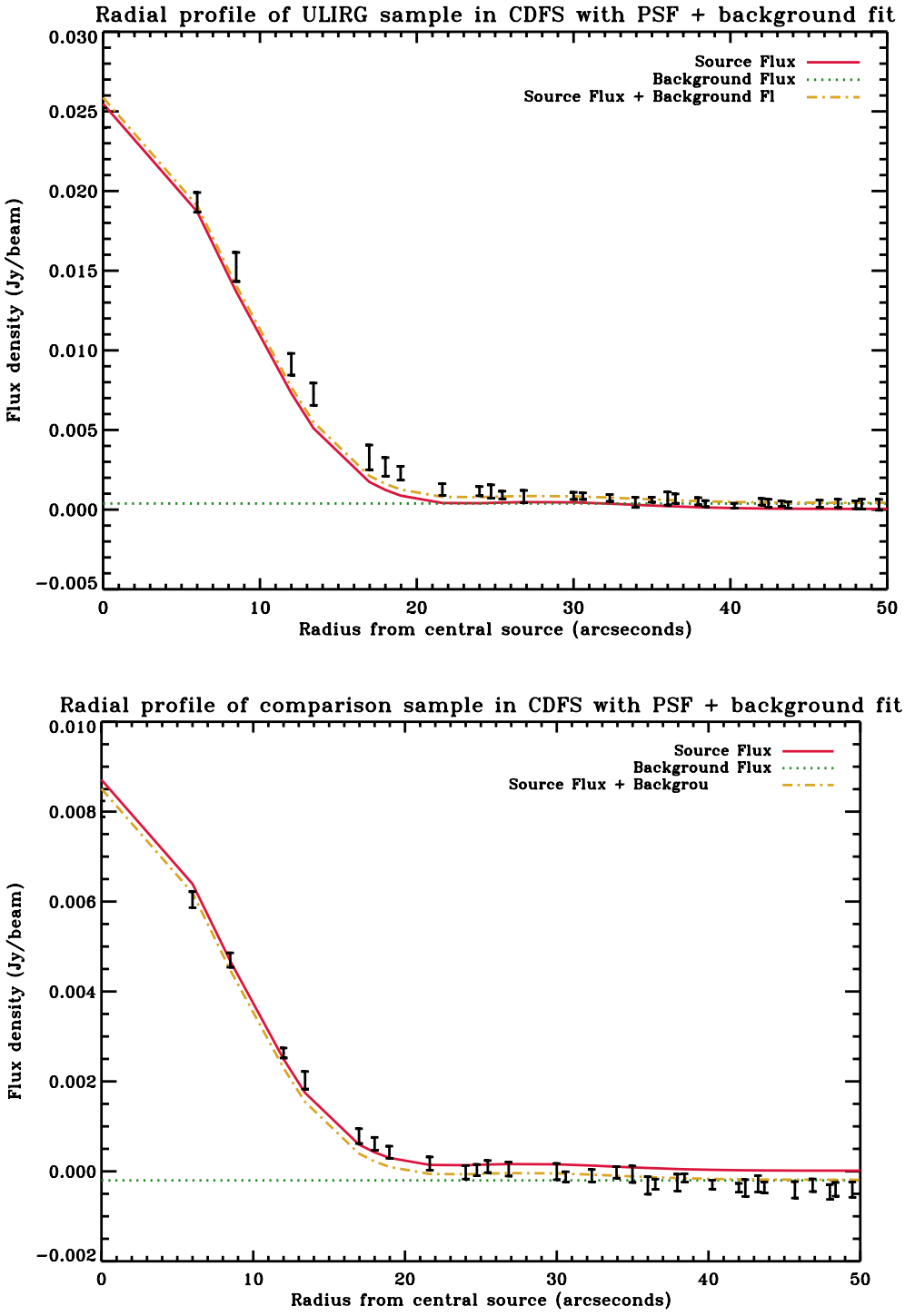

Figure 4.4: 1D radial profiles of the stacked sources for the 24μm bright (top) and 24μm faint (bottom) samples in CDFS. The data points are the flux densities at different radii from the stacked 250μm images. Error bars are calculated from the standard deviation of all points at the same radii. A model containing the PSF of the central source plus a constant background is fit to the data. The red line represents the PSF; the green dotted line, the background; and the yellow dot-dashed line shows the PSF plus the background.

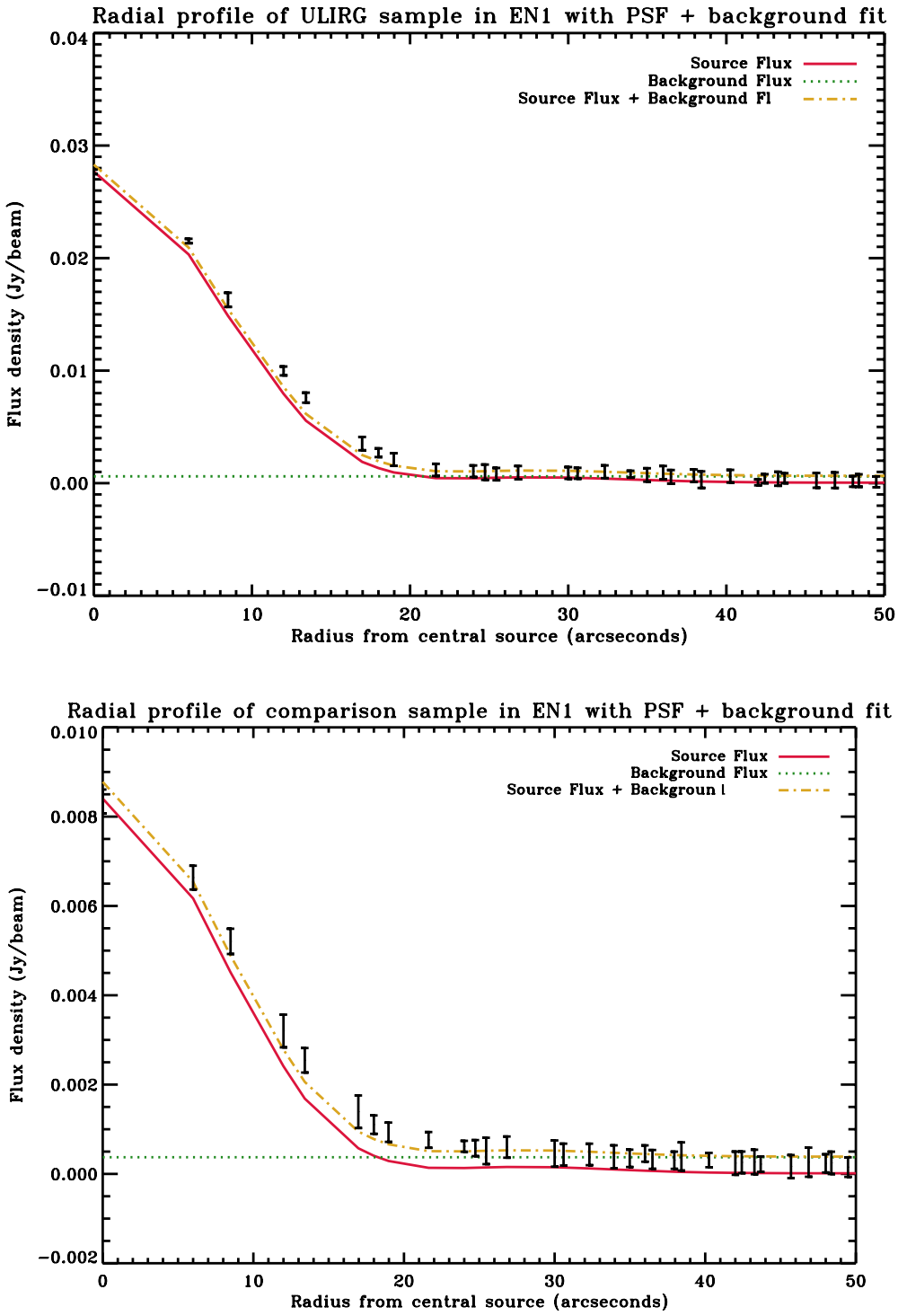

Figure 4.5: 1D radial profiles of the stacked sources for the 24μm bright (top) and 24μm faint (bottom) samples in EN1. The data points are the flux densities at different radii from the stacked 250μm images. Error bars are calculated from the standard deviation of all points at the same radii. A model containing the PSF of the central source plus a constant background is fit to the data. The red line represents the PSF; the green dotted line, the background; and the yellow dot-dashed line shows the PSF plus the background.

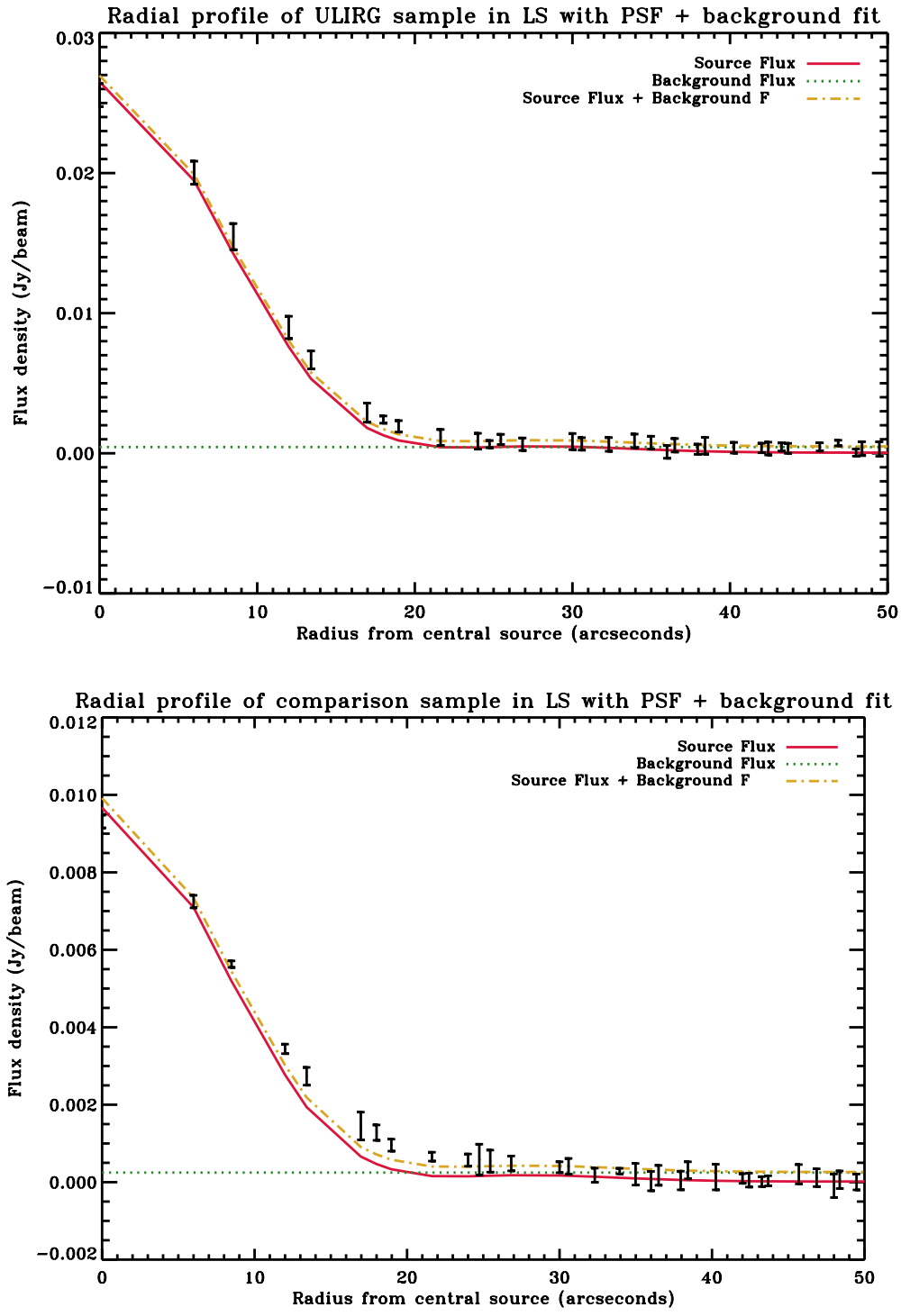

Figure 4.6: 1D radial profiles of the stacked sources for the 24μm bright (top) and 24μm faint (bottom) samples in LS. The data points are the flux densities at different radii from the stacked 250μm images. Error bars are calculated from the standard deviation of all points at the same radii. A model containing the PSF of the central source plus a constant background is fit to the data. The red line represents the PSF; the green dotted line, the background; and the yellow dot-dashed line shows the PSF plus the background.

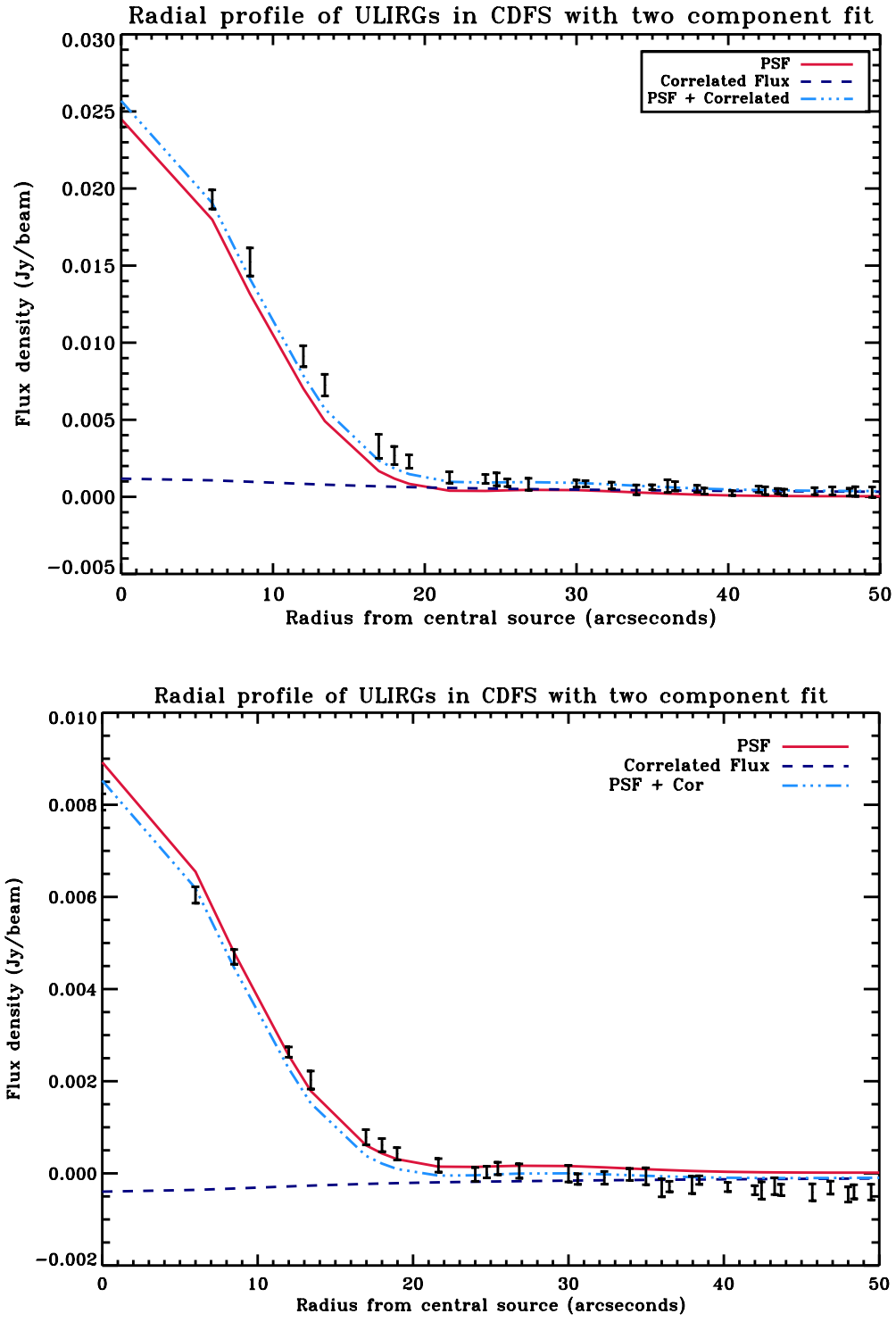

Figure 4.7: 1D radial profiles of the stacked sources for the 24μm bright (top) and 24μm faint (bottom) samples in CDFS. The data points are the flux densities at different radii from the stacked 250μm images. Error bars are calculated from the standard deviation of all points at the same radii. A model containing the PSF of the central source, plus the correlation function, w_θ, is fit to the data. The red line represents the PSF; the dark blue dashed line, the correlated flux; and the light blue dot-dashed line shows the PSF plus the correlated flux.

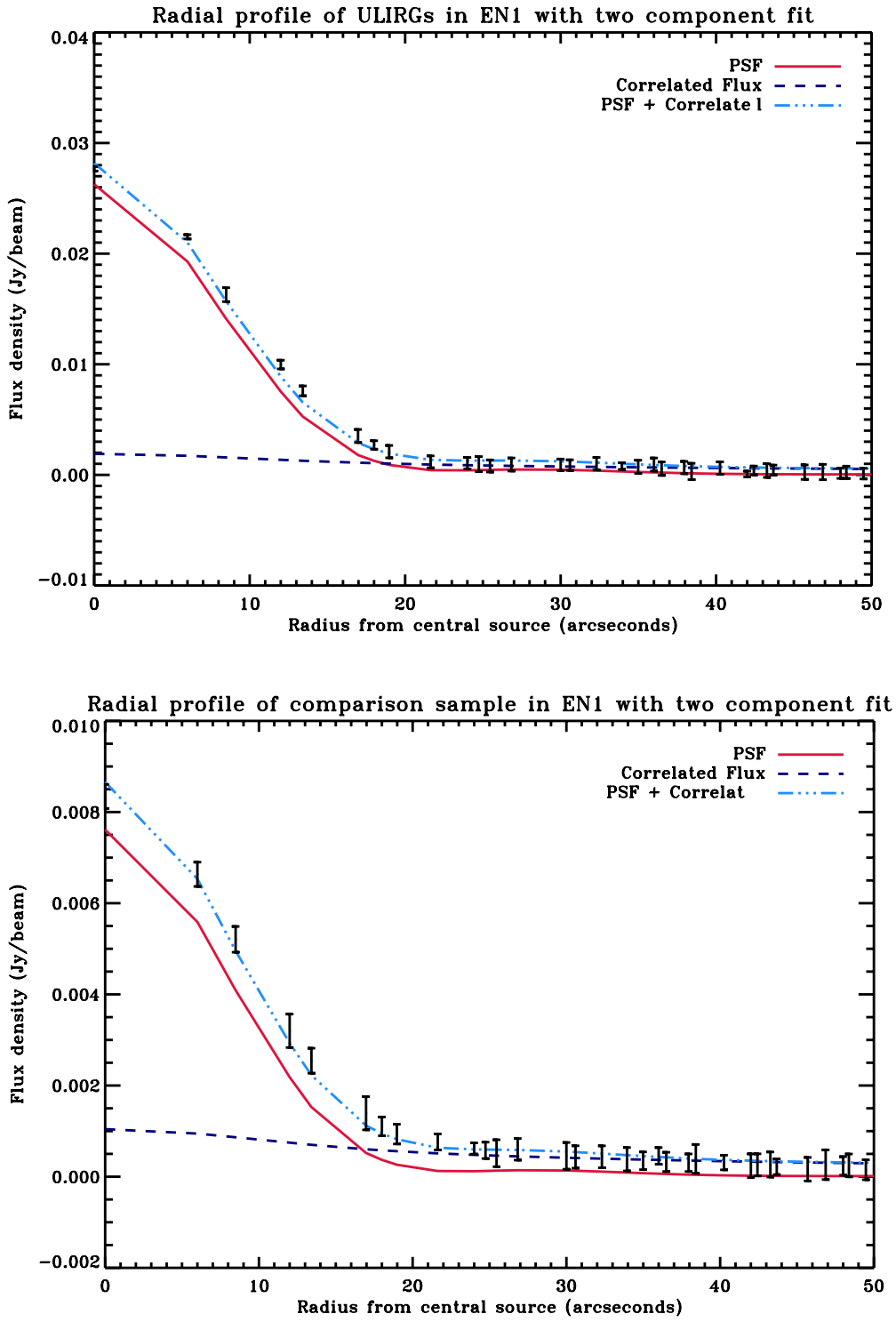

Figure 4.8: 1D radial profiles of the stacked sources for the 24μm bright (top) and 24μm faint (bottom) samples in EN1. The data points are the flux densities at different radii from the stacked 250μm images. Error bars are calculated from the standard deviation of all points at the same radii. A model containing the PSF of the central source, plus the correlation function, w$_\theta$, is fit to the data. The red line represents the PSF; the dark blue dashed line, the correlated flux; and the light blue dot-dashed line shows the PSF plus the correlated flux.

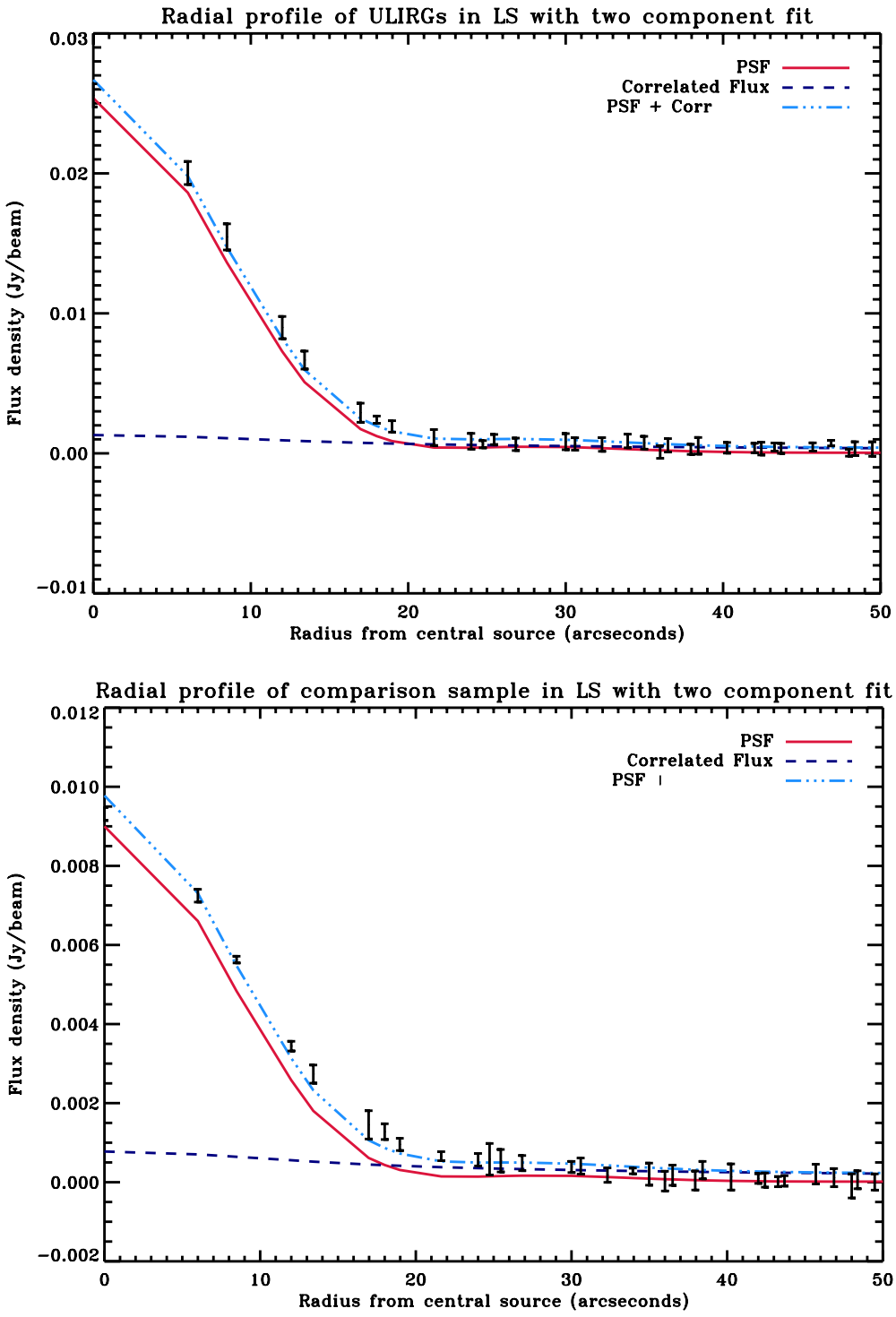

Figure 4.9: 1D radial profiles of the stacked sources for the 24μm bright (top) and 24μm faint (bottom) samples in LS. The data points are the flux densities at different radii from the stacked 250μm images. Error bars are calculated from the standard deviation of all points at the same radii. A model containing the PSF of the central source, plus the correlation function, w$_\theta$, is fit to the data. The red line represents the PSF; the dark blue dashed line, the correlated flux; and the light blue dot-dashed line shows the PSF plus the correlated flux.

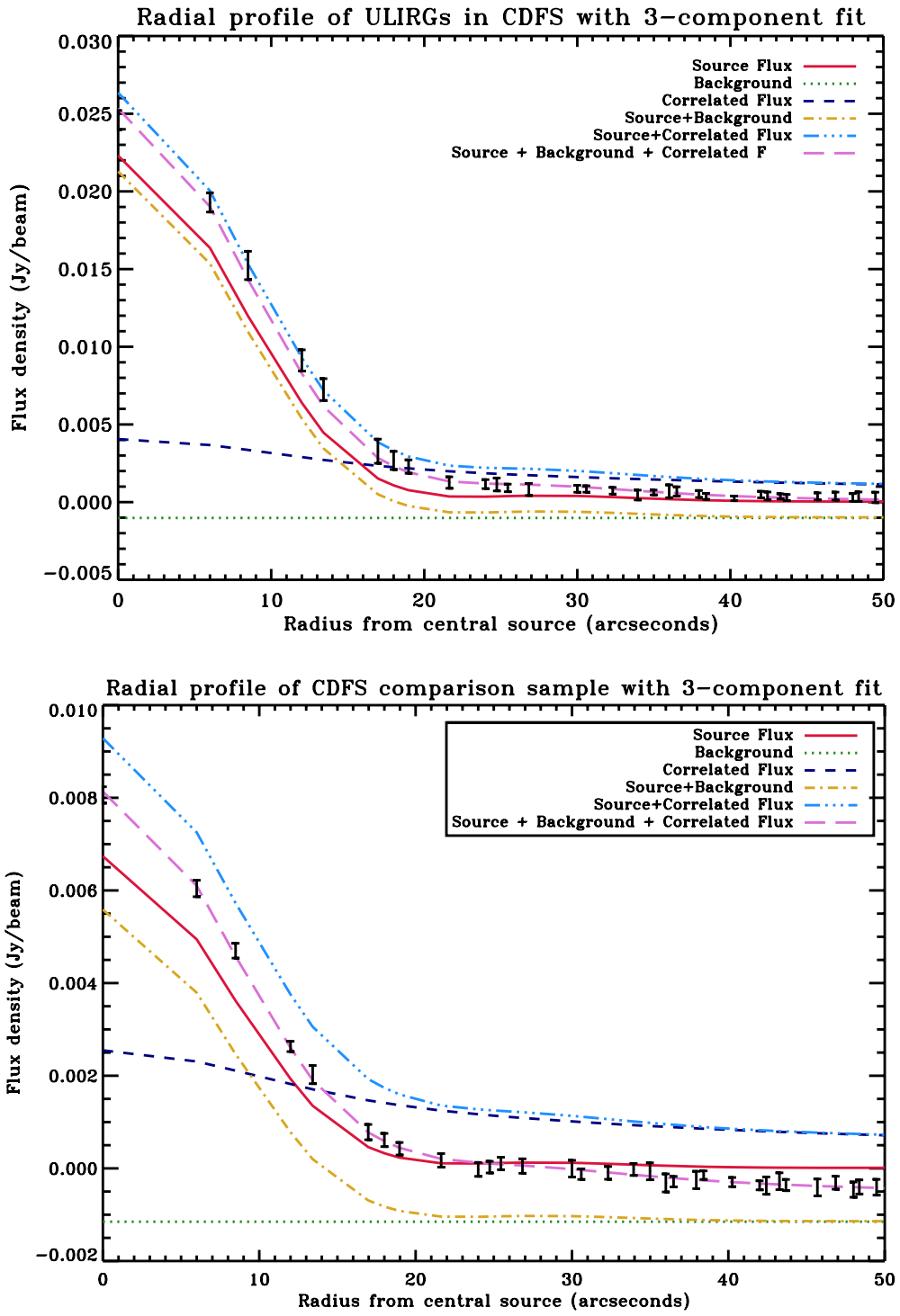

Figure 4.10: 1D radial profiles of the stacked sources for the 24μm bright (top) and 24μm faint (bottom) samples in CDFS. The data points are the flux densities at different radii from the stacked 250μm images. Error bars are calculated from the standard deviation of all points at the same radii. A three-component model containing the PSF of the central source, a correlation function, w_θ, and a constant background is fit to the data. The red line represents the PSF; the dark blue dashed line, the correlated flux; and the green dotted line shows the background. The yellow dot-dashed line represents the PSF plus the background; the light blue dot-dashed line, the PSF plus the correlated flux; and all three components are given by the purple dashed line.

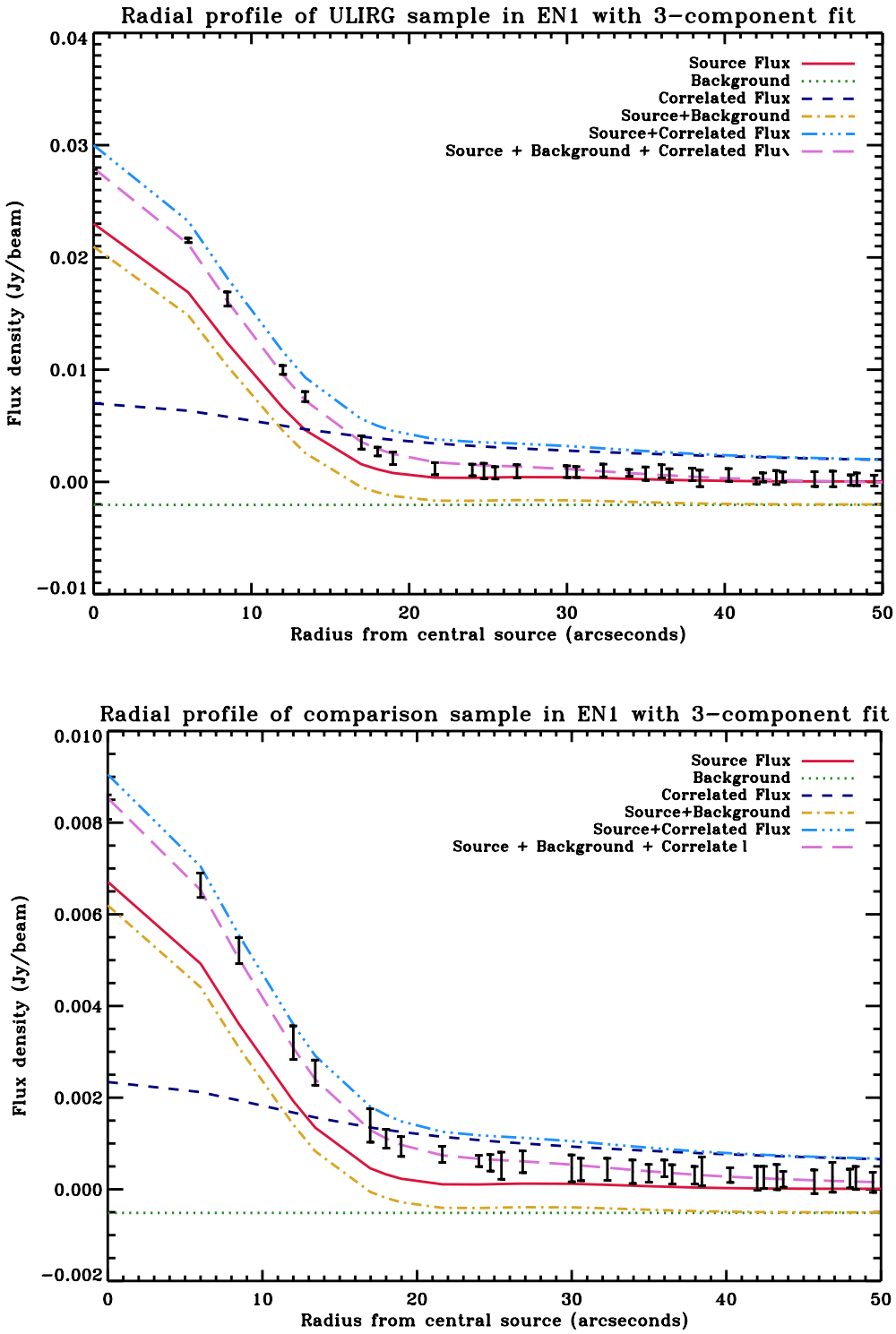

Figure 4.11: 1D radial profiles of the stacked sources for the 24μm bright (top) and 24μm faint (bottom) samples in EN1. The data points are the flux densities at different radii from the stacked 250μm images. Error bars are calculated from the standard deviation of all points at the same radii. A three-component model containing the PSF of the central source, a correlation function, w_θ, and a constant background is fit to the data. The red line represents the PSF; the dark blue dashed line, the correlated flux; and the green dotted line shows the background. The yellow dot-dashed line represents the PSF plus the background; the light blue dot-dashed line, the PSF plus the correlated flux; and all three components are given by the purple dashed line.

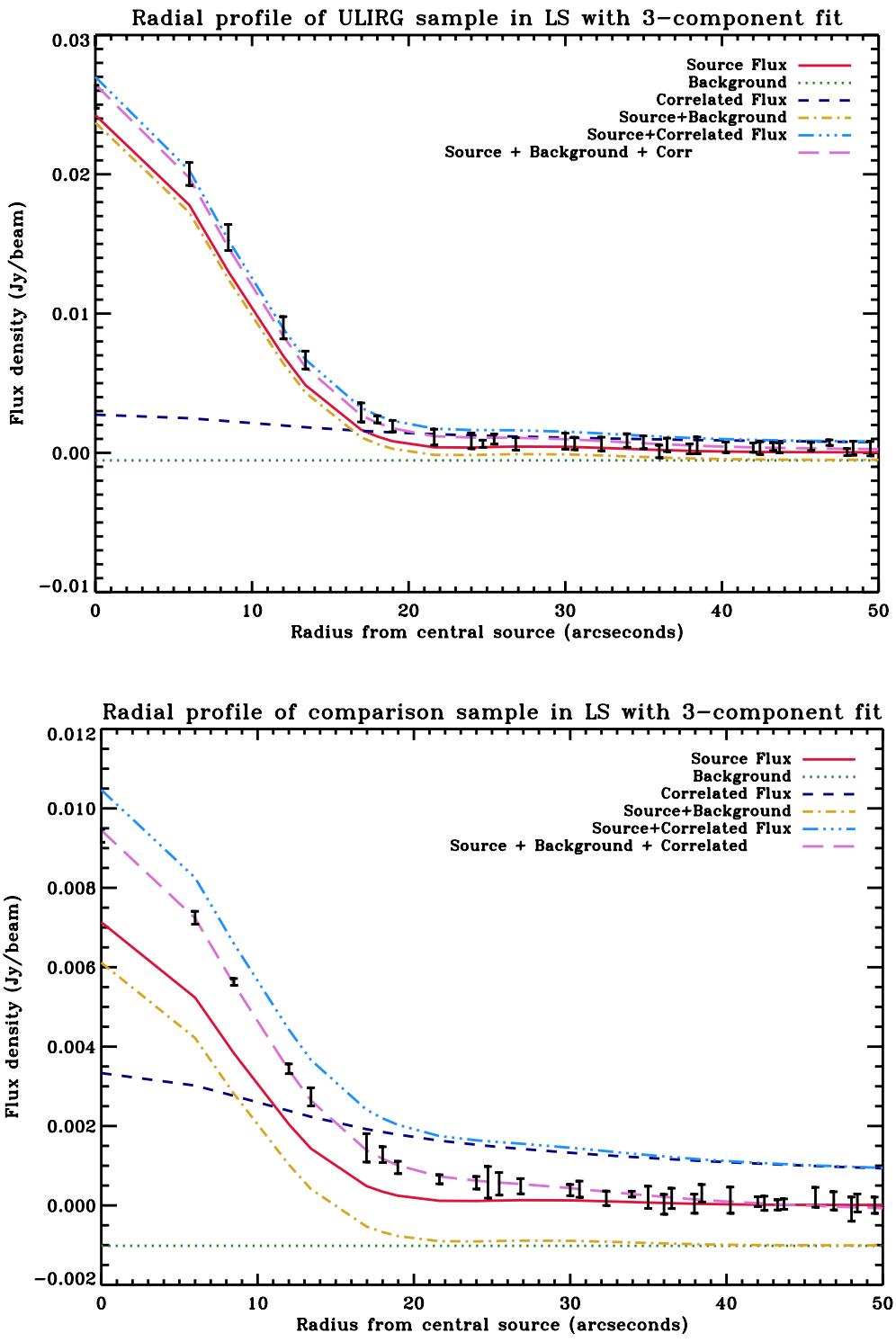

Figure 4.12: 1D radial profiles of the stacked sources for the 24μm bright (top) and 24μm faint (bottom) samples in LS. The data points are the flux densities at different radii from the stacked 250μm images. Error bars are calculated from the standard deviation of all points at the same radii. A three-component model containing the PSF of the central source, a correlation function, w_θ, and a constant background is fit to the data. The red line represents the PSF; the dark blue dashed line, the correlated flux; and the green dotted line shows the background. The yellow dot-dashed line represents the PSF plus the background; the light blue dot-dashed line, the PSF plus the correlated flux; and all three components are given by the purple dashed line.

4.2 Star Formation in Correlated Sources

From the above, the models containing a correlated component are found to fit best to the data from the stack. In order to quantify the flux density originating from the correlated sources, the PSF model image was scaled and subtracted from the stacked image, to obtain the residual flux density remaining. The sum of this was then taken to give the total flux density arising from these objects. The units of this quantity are changed from the map units of Jy/beam to Jy by dividing the integrated correlated flux by the integrated PSF flux, since the PSF at the centre of the image has a value of unity. As a test of the accuracy of this result, these values are compared to those obtained from integrating under the model correlation function curve, which should yield the total flux from the correlated sources. The model chosen as being the best fit was that containing the two components of the PSF and correlated flux, as the background was coming out as negative from the fitting. The minimisation algorithm used was the Levenberg-Marquardt method. Using the starburst models of Efstathiou et al (2000), the typical 250μm flux of a ULIRG at z 2 with a 24μm flux of 350μJy is 15 mJy +/-10 mJy. Thus, assuming that these starburst models accurately represent star formation in high redshift ULIRGs, approximately 2% of the sample should be directly detected.

In order to obtain luminosities, a template spectrum was then fit to the objects. The spectrum used was that of M82 from the SPIRE template library (Polletta et al., 2007). We sum the area under the spectrum between 8 and 1000 μm in order to obtain the total FIR correlated flux density F. This is converted to a FIR luminosity, L, using the relation $L = 4\pi d^2 F$, where d is the luminosity distance at $z = 1.7$. We extrapolate from far-infrared (FIR) luminosities to star formation rates (SFRs) using the relation of Oliver et al. (2010) for infrared selected starburst galaxies:

$$\frac{SFR}{M_{\odot} yr^{-1}} = \frac{L_{FIR}/L_{\odot}}{0.51 \times 10^{10}} \tag{4.1}$$

The flux densities, luminosities and star formation rates obtained using this method are shown in Table 4.2. From the above, the star formation rate densities can be determined, which gives the star formation rate per unit volume. This is a useful quantity for probing the cosmic star formation history. To ascertain the star formation rate densities from the correlated sources, the volume of a sphere is taken at the maximum radius at redshift 1.7, and the excess flux is divided by this, with the assumption that this excess is all at the redshift of the objects. The volume of a sphere of radius 1 Mpc is

$$V = \frac{4}{3}\pi(1Mpc)^3 = 4.189Mpc^3. \tag{4.2}$$

Object Type	Field	Integrated Correlated Flux Density (Jy)	Image Residual Flux Density (Jy)	Luminosity ($L_\odot$)	Star Formation Rate ($M_\odot yr^{-1}$)	Star Formation Rate Density ($M_\odot yr^{-1} Mpc^{-3}$)
	CDFS	0.12304	0.02319	3855	7.5331	1.7983
24μm flux >350μJy	EN1	0.1444	0.01608	6223	12.1617	2.9032
	LS	0.0989	0.01784	4263	8.3314	1.9888
	CDFS	-0.0300	-0.02738	-1295	-2.5302	-0.60401
24μm flux <350μJy	EN1	0.0789	0.00712	4263	6.6509	1.5877
	LS	0.0588	0.00649	2534	4.9512	1.1819

Table 4.3: Flux densities, FIR luminosities and star formation rates of the correlated sources at 250μm.

Chapter 5

Conclusions and Future Work

5.1 Conclusion

We have investigated bump ULIRGs in order to ascertain whether these objects have excess flux in their environments, since members of this class of galaxy are likely to be hosted in overdense, massive dark matter halos, in which a greater rate of star formation would be expected compared to average density regions. Our main conclusions are summarised as follows:

1. Both the objects with 24μm flux $> 350\mu$Jy and the comparison sample were best fit by a model containing a component of correlated flux in addition to the point spread function of the objects.

2. This evidence is stronger for the sample of objects which have a higher 24μm flux density as the amount of this correlated flux was greater for these objects in all three fields.

3. There is therefore some evidence that companion objects are present in the local environments of these galaxies.

4. The excess flux corresponds to a star formation rate density that is of the order of $1\mathrm{M}_{\odot}\mathrm{yr}^{-1}\mathrm{Mpc}^{3}$.

Evidence such as this for a component of flux that is coming from correlated sources for both samples would be expected if these objects reside in massive dark matter haloes. This could appear to indicate that the observed excess of submm flux in their environments is arising from obscured star formation from companion objects that are in a protocluster environment.

During the completion of this thesis, the Herschel Space Observatory came to the natural end of its mission lifetime. On April 29th, 2013, its onboard helium reservoir was depleted, with the subsequent rise in temperature of all the instruments rendering further observations impossible.

The proposed next generation infrared space telescope, named the Space Infra-Red Telescope for Cosmology and Astrophysics (SPICA, Nakagawa (2004)), is currently planned for launch in 2025, to continue our exploration into the infrared universe.

5.2 Future Work

5.2.1 Extension to all SPIRE bands and production of a stacked SED

A next step to this project would be to complete the current analysis by applying the same method using data at the other two SPIRE wavelengths, 350 and 500 μm. This would enable a comparison with the results at 250 μm, in order to check whether the ratio of the fluxes are consistent. A stack of the Spitzer bands along with those at 350 and 500 μm would make it possible to fit models for star formation across these wavelengths.

5.2.2 Analysis at 24 microns

A similar technique could be applied to analyse the environments of these sources at 24 μm using data from Spitzer. This would expand our knowledge of these objects because the 24 μm data is a tracer of star formation. At this redshift, features from PAHs are redshifted into the MIPS bands, and detection of these would indicate the presence of massive stars.

5.2.3 Search for bump-2 sources and their directly detected companions

A similar search could also be conducted in the Herschel and Spitzer images to look for directly detected companions to these sources, and a similar analysis of their properties could be performed. This could show whether any of the detected companions dominate the stacked radial profiles. If bump-2 sources signpost overdensities, then we would expect to see companions. Herschel and deep K-band observations may show these companions already in the process of forming, and could give an indication of how fast they are forming stars, providing another source of evidence that they are in overdense regions.

5.2.4 Follow-up observations

Follow-up observations could be conducted on these sources using ground-based facilities such as the James Clerk Maxwell telescope (JCMT), the Atacama Large Millimetre Array (ALMA), and the Plateau de Bure interferometer (PdBI), as well as with optical and near-IR telescopes. In particular, the PdBI could be used to carry out carbon monoxide (CO) interferometry, as CO is an inevitable byproduct of star formation during the carbon-nitrogen-oxygen cycle of fusion in stellar

cores. CO lines could then be searched for as independent traces of star formation. By looking at multiple lines and estimating the amount of CO remaining, a determination could be made of the total mass of CO and how long the star formation will last for. This also could be carried out using ALMA, which has better resolution, but its view is limited, whereas the PdBI is able to view any part of the sky. ALMA could be useful in providing very high-resolution imaging at 850 μm, as this allows multiple tests and checks of whether all of the Herschel flux is originating from bump-2 sources.

5.2.5 Other objects

A further extension of this work could then perform a similar analysis on other classes of objects which are expected to reside in overdense regions, such as quasars and radio galaxies, in an attempt to quantify the star formation occurring in a range of halo masses and redshifts.

Bibliography

Armus, L., Charmandaris, V., Bernard-Salas, J., Spoon, H. W. W., Marshall, J. A., Higdon, S. J. U., Desai, V., Teplitz, H. I., Hao, L., Devost, D., Brandl, B. R., Wu, Y., Sloan, G. C., Soifer, B. T., Houck, J. R., and Herter, T. L. (2007). Observations of Ultraluminous Infrared Galaxies with the Infrared Spectrograph on the Spitzer Space Telescope. II. The IRAS Bright Galaxy Sample. *The Astrophysical Journal*, 656:148–167. 11

Bavouzet, N. (2009). *Infrared Galaxies : Spatial Distribution, Contribution to the Extragalactic Background and Spectral Energy Distribution*. PhD thesis, Institut d'Astrophysique Spatiale. 18

Béthermin, M., Dole, H., Beelen, A., and Aussel, H. (2010). Spitzer deep and wide legacy mid- and far-infrared number counts and lower limits of cosmic infrared background*. *A&A*, 512:A78. 18

Blain, A. W., Chapman, S. C., Smail, I., and Ivison, R. (2004). Clustering of Submillimeter-selected Galaxies. *The Astrophysical Journal*, 611:725–731. 13

Blain, A. W., Smail, I., Ivison, R. J., Kneib, J.-P., and Frayer, D. T. (2002). Submillimeter galaxies. *Physics Reports*, 369:111–176. 11

Condon, J. (1992). Radio emission from normal galaxies. *Annual Review of Astronomy and Astrophysics*, 30:575–611. 11

de Graauw, T., Helmich, F. P., Phillips, T. G., Stutzki, J., Caux, E., Whyborn, N. D., Dieleman, P., Roelfsema, P. R., Aarts, H., Assendorp, R., Bachiller, R., Baechtold, W., Barcia, A., Beintema, D. A., Belitsky, V., Benz, A. O., Bieber, R., Boogert, A., Borys, C., Bumble, B., Caïs, P., Caris, M., Cerulli-Irelli, P., Chattopadhyay, G., Cherednichenko, S., Ciechanowicz, M., Coeur-Joly, O., Comito, C., Cros, A., de Jonge, A., de Lange, G., Delforges, B., Delorme, Y., den Boggende, T., Desbat, J.-M., Diez-González, C., di Giorgio, A. M., Dubbeldam, L., Edwards, K., Eggens, M., Erickson, N., Evers, J., Fich, M., Finn, T., Franke, B., Gaier, T., Gal, C., Gao,

J. R., Gallego, J.-D., Gauffre, S., Gill, J. J., Glenz, S., Golstein, H., Goulooze, H., Gunsing, T., Güsten, R., Hartogh, P., Hatch, W. A., Higgins, R., Honingh, E. C., Huisman, R., Jackson, B. D., Jacobs, H., Jacobs, K., Jarchow, C., Javadi, H., Jellema, W., Justen, M., Karpov, A., Kasemann, C., Kawamura, J., Keizer, G., Kester, D., Klapwijk, T. M., Klein, T., Kollberg, E., Kooi, J., Kooiman, P.-P., Kopf, B., Krause, M., Krieg, J.-M., Kramer, C., Kruizenga, B., Kuhn, T., Laauwen, W., Lai, R., Larsson, B., Leduc, H. G., Leinz, C., Lin, R. H., Liseau, R., Liu, G. S., Loose, A., López-Fernandez, I., Lord, S., Luinge, W., Marston, A., Martín-Pintado, J., Maestrini, A., Maiwald, F. W., McCoey, C., Mehdi, I., Megej, A., Melchior, M., Meinsma, L., Merkel, H., Michalska, M., Monstein, C., Moratschke, D., Morris, P., Muller, H., Murphy, J. A., Naber, A., Natale, E., Nowosielski, W., Nuzzolo, F., Olberg, M., Olbrich, M., Orfei, R., Orleanski, P., Ossenkopf, V., Peacock, T., Pearson, J. C., Peron, I., Phillip-May, S., Piazzo, L., Planesas, P., Rataj, M., Ravera, L., Risacher, C., Salez, M., Samoska, L. A., Saraceno, P., Schieder, R., Schlecht, E., Schlöder, F., Schmülling, F., Schultz, M., Schuster, K., Siebertz, O., Smit, H., Szczerba, R., Shipman, R., Steinmetz, E., Stern, J. A., Stokroos, M., Teipen, R., Teyssier, D., Tils, T., Trappe, N., van Baaren, C., van Leeuwen, B.-J., van de Stadt, H., Visser, H., Wildeman, K. J., Wafelbakker, C. K., Ward, J. S., Wesselius, P., Wild, W., Wulff, S., Wunsch, H.-J., Tielens, X., Zaal, P., Zirath, H., Zmuidzinas, J., and Zwart, F. (2010). The Herschel-Heterodyne Instrument for the Far-Infrared (HIFI). *Astronomy and Astrophysics*, 518:L6. 7

de Vaucouleurs, G. (1959). Classification and Morphology of External Galaxies. *Handbuch der Physik*, 53:275. 1

Deza, M. M. and Deza, E. (2012). *Encyclopedia of Distances*. Springer. 3

Elmegreen, D. M. and Elmegreen, B. G. (1982). Flocculent and grand design spiral structure in field, binary and group galaxies. *Monthly Notices of the Royal Astronomical Society*, 201:1021. 1

Farrah, D., Afonso, J., Efstathiou, A., Rowan-Robinson, M., Fox, M., and Clements, D. (2003). Starburst and AGN activity in ultraluminous infrared galaxies. *Monthly Notices of the Royal Astronomical Society*, 343:585607. 11

Farrah, D., Bernard-Salas, J., Spoon, H. W. W., Soifer, B. T., Armus, L., Brandl, B., Charmandaris, V., Desai, V., Higdon, S., Devost, D., and Houck, J. (2007). High-Resolution Mid-Infrared Spectroscopy of Ultraluminous Infrared Galaxies. *The Astrophysical Journal*, 667:149–169. 11

Farrah, D., Lonsdale, C. J., Weedman, D. W., Spoon, H. W. W., Rowan-Robinson, M., Poletta,

M., Oliver, S., Houck, J. R., and Smith, H. E. (2008). The Nature of Star Formation in Distant Ultraluminous Infrared Galaxies Selected in a Remarkably Narrow Redshift Range. *The Astrophysical Journal*, 677:957–969. 15, 16

Fazio, G. et al. (2004). The Infrared Array Camera (IRAC) for the Spitzer Space Telescope. *The Astrophysical Journal Supplement Series*, 154:10–17. 6

Franceschini, A., Braito, V., Persic, M., Della Ceca, R., Bassani, L., Cappi, M., Malaguti, P., Palumbo, G. G. C., Risaliti, G., Salvati, M., and Severgnini, P. (2003). An XMM-Newton hard survey of ultraluminous infrared galaxies. *Monthly Notices of the Royal Astronomical Society*, 343:1181–1194. 11

Griffin, M. J., Abergel, A., Abreu, A., Ade, P. A. R., André, P., Augueres, J.-L., Babbedge, T., Bae, Y., Baillie, T., Baluteau, J.-P., Barlow, M. J., Bendo, G., Benielli, D., Bock, J. J., Bonhomme, P., Brisbin, D., Brockley-Blatt, C., Caldwell, M., Cara, C., Castro-Rodriguez, N., Cerulli, R., Chanial, P., Chen, S., Clark, E., Clements, D. L., Clerc, L., Coker, J., Communal, D., Conversi, L., Cox, P., Crumb, D., Cunningham, C., Daly, F., Davis, G. R., de Antoni, P., Delderfield, J., Devin, N., di Giorgio, A., Didschuns, I., Dohlen, K., Donati, M., Dowell, A., Dowell, C. D., Duband, L., Dumaye, L., Emery, R. J., Ferlet, M., Ferrand, D., Fontignie, J., Fox, M., Franceschini, A., Frerking, M., Fulton, T., Garcia, J., Gastaud, R., Gear, W. K., Glenn, J., Goizel, A., Griffin, D. K., Grundy, T., Guest, S., Guillemet, L., Hargrave, P. C., Harwit, M., Hastings, P., Hatziminaoglou, E., Herman, M., Hinde, B., Hristov, V., Huang, M., Imhof, P., Isaak, K. J., Israelsson, U., Ivison, R. J., Jennings, D., Kiernan, B., King, K. J., Lange, A. E., Latter, W., Laurent, G., Laurent, P., Leeks, S. J., Lellouch, E., Levenson, L., Li, B., Li, J., Lilienthal, J., Lim, T., Liu, S. J., Lu, N., Madden, S., Mainetti, G., Marliani, P., McKay, D., Mercier, K., Molinari, S., Morris, H., Moseley, H., Mulder, J., Mur, M., Naylor, D. A., Nguyen, H., O'Halloran, B., Oliver, S., Olofsson, G., Olofsson, H.-G., Orfei, R., Page, M. J., Pain, I., Panuzzo, P., Papageorgiou, A., Parks, G., Parr-Burman, P., Pearce, A., Pearson, C., Pérez-Fournon, I., Pinsard, F., Pisano, G., Podosek, J., Pohlen, M., Polehampton, E. T., Pouliquen, D., Rigopoulou, D., Rizzo, D., Roseboom, I. G., Roussel, H., Rowan-Robinson, M., Rownd, B., Saraceno, P., Sauvage, M., Savage, R., Savini, G., Sawyer, E., Scharmberg, C., Schmitt, D., Schneider, N., Schulz, B., Schwartz, A., Shafer, R., Shupe, D. L., Sibthorpe, B., Sidher, S., Smith, A., Smith, A. J., Smith, D., Spencer, L., Stobie, B., Sudiwala, R., Sukhatme, K., Surace, C., Stevens, J. A., Swinyard, B. M., Trichas, M., Tourette, T., Triou, H., Tseng, S., Tucker, C., Turner, A., Vaccari, M., Valtchanov, I., Vigroux, L., Virique, E., Voellmer, G., Walker, H., Ward, R., Waskett, T., Weilert, M., Wesson, R., White, G. J., Whitehouse, N., Wilson, C. D.,

Winter, B., Woodcraft, A. L., Wright, G. S., Xu, C. K., Zavagno, A., Zemcov, M., Zhang, L., and Zonca, E. (2010). The Herschel-SPIRE instrument and its in-flight performance. *Astronomy and Astrophysics*, 518:L3. 7

HERSCHEL-DOC-0798 (2011). *SPIRE Observer's Manual*. version 2.3. 20

Hopkins, P. F., Younger, J. D., Hayward, C. C., Narayanan, D., and Hernquist, L. (2010). Mergers, active galactic nuclei and normal galaxies: contributions to the distribution of star formation rates and infrared luminosity functions. *Monthly Notices of the Royal Astronomical Society*, 402(3):1693–1713. 13

Houck, J. R., Roellig, T. L., van Cleve, J., Forrest, W. J., Herter, T., Lawrence, C. R., Matthews, K., Reitsema, H. J., Soifer, B. T., Watson, D. M., Weedman, D., Huisjen, M., Troeltzsch, J., Barry, D. J., Bernard-Salas, J., Blacken, C. E., Brandl, B. R., Charmandaris, V., Devost, D., Gull, G. E., Hall, P., Henderson, C. P., Higdon, S. J. U., Pirger, B. E., Schoenwald, J., Sloan, G. C., Uchida, K. I., Appleton, P. N., Armus, L., Burgdorf, M. J., Fajardo-Acosta, S. B., Grillmair, C. J., Ingalls, J. G., Morris, P. W., and Teplitz, H. I. (2004). The Infrared Spectrograph (IRS) on the Spitzer Space Telescope. *The Astrophysical Journal Supplement Series*, 154:18–24. 6

Hubble, E. P. (1926). Extragalactic Nebulae. *The Astrophysical Journal*, 64:321. 1

Hubble, E. P. (1936). *Realm of the Nebulae*. New Haven: Yale University Press. 1

Kennicutt, R. (1992). A Spectrophotometric Atlas of Galaxies. *The Astrophysical Journal Supplement Series*, 79:255–284. 8

Kim, D.-C., Veilleux, S., and Sanders, D. B. (1998). The IRAS 1 Jy Sample of Ultraluminous Infrared Galaxies. II. Optical Spectroscopy. *The Astrophysical Journal*, 508:627–647. 11

Lagache, G., Puget, J.-L., and Dole, H. (2005). Dusty Infrared Galaxies: Sources of the Cosmic Infrared Background. *Annual Review of Astronomy and Astrophysics*, 43:727–768. 11

Le Floc'h, E., Papovich, C., Dole, H., Bell, E. F., Lagache, G., Rieke, G. H., Egami, E., Pérez-Gonzalez, P. G., Alonso-Herrero, A., Rieke, M. J., Blaylock, M., Engelbracht, C. W., Gordon, K. D., Hines, D. C., Misselt, K. A., Morrison, J. E., and Mould, J. (2005). Infrared Luminosity Functions from the Chandra Deep Field South: The Spitzer View on the History of Dusty Star Formation at $0<z<1$. *The Astrophysical Journal*, 632:169–190. 11

Lonsdale, C. J. (2006). Ultraluminous Infrared Galaxies. In Mason, J., editor, *Astrophysics Update 2*, page 285. Springer Verlag. 11

Lonsdale, C. J., Smith, H. E., Rowan-Robinson, M., Surace, J., Shupe, D., Xu, C., Oliver, S., Padgett, D., Fang, F., Conrow, T., Franceschini, A., Gautier, N., Griffin, M., Hacking, P., Masci, F., Morrison, G., O'Linger, J., Owen, F., Pérez-Fournon, I., Pierre, M., Puetter, R., Stacey, G., Castro, S., Polletta, M. d. C., Farrah, D., Jarrett, T., Frayer, D., Siana, B., Babbedge, T., Dye, S., Fox, M., Gonzalez-Solares, E., Salaman, M., Berta, S., Condon, J. J., Dole, H., and Serjeant, S. (2003). SWIRE: The SIRTF Wide-Area Infrared Extragalactic Survey. *Publications of the Astronomical Society of the Pacific*, 115:897–927. 6

Maller, A. H., McIntosh, D. H., Katz, N., and Weinberg, M. D. (2005). The galaxy angular correlation functions and power spectrum from the two micron all sky survey. *The Astrophysical Journal*, 619:147–160. 20

Marcillac, D., Rieke, G. H., Papovich, C., Willmer, C. N. A., Weiner, B. J., Coil, A. L., Cooper, M. C., Gerke, B. F., Woo, J., Newman, J. A., Georgakakis, A., Laird, E. S., Nandra, K., Fazio, G. G., Huang, J.-S., and Koo, D. C. (2008). The Environment on a Few Mpc Scales of Infrared Luminous Galaxies at Redshift z 1. *The Astrophysical Journal*, 675:1156. 13

Morgan, W. (1958). A Preliminary Classification of the Forms of Galaxies According to Their Stellar Population. *Publications of the Astronomical Society of the Pacific*, 70:364. 1

Nakagawa, T. (2004). SPICA: space infrared telescope for cosmology and astrophysics. *Advances in Space Research*, 34:645650. 41

Neugebauer, G., Habing, H. J., van Duinen, R., Aumann, H. H., Baud, B., Beichman, C. A., Beintema, D. A., Boggess, N., Clegg, P. E., de Jong, T., Emerson, J. P., Gautier, T. N., Gillett, F. C., Harris, S., Hauser, M. G., Houck, J. R., Jennings, R. E., Low, F. J., Marsden, P. L., Miley, G., Olnon, F. M., Pottasch, S. R., Raimond, E., Rowan-Robinson, M., Soifer, B. T., Walker, R. G., Wesselius, P. R., and Young, E. (1984). The Infrared Astronomical Satellite (IRAS) mission. *The Astrophysical Journal Letters*, 278:L1–L6. 5

Oliver, S., Frost, M., Farrah, D., Gonzalez-Solares, E., Shupe, D. L., Henriques, B., Roseboom, I., Alfonso-Luis, A., Babbedge, T. S. R., Frayer, D., Lencz, C., Lonsdale, C. J., Masci, F., Padgett, D., Polletta, M., Rowan-Robinson, M., Siana, B., Smith, H. E., Surace, J. A., and Vaccari, M. (2010). Specific star formation and the relation to stellar mass from $0 < z < 2$ as seen in the far-infrared at 70 and 160 μm. *Monthly Notices of the Royal Astronomical Society*, 405:2279–2294. 38

Oliver, S. J., Bock, J., Altieri, B., Amblard, A., Arumugam, V., Aussel, H., Babbedge, T., Beelen, A., Béthermin, M., Blain, A., Boselli, A., Bridge, C., Brisbin, D., Buat, V., Burgarella, D.,

Castro-Rodríguez, N., Cava, A., Chanial, P., Cirasuolo, M., Clements, D. L., Conley, A., Conversi, L., Cooray, A., Dowell, C. D., Dubois, E. N., Dwek, E., Dye, S., Eales, S., Elbaz, D., Farrah, D., Feltre, A., Ferrero, P., Fiolet, N., Fox, M., Franceschini, A., Gear, W., Giovannoli, E., Glenn, J., Gong, Y., González Solares, E. A., Griffin, M., Halpern, M., Harwit, M., Hatziminaoglou, E., Heinis, S., Hurley, P., Hwang, H. S., Hyde, A., Ibar, E., Ilbert, O., Isaak, K., Ivison, R. J., Lagache, G., Le Floc'h, E., Levenson, L., Faro, B. L., Lu, N., Madden, S., Maffei, B., Magdis, G., Mainetti, G., Marchetti, L., Marsden, G., Marshall, J., Mortier, A. M. J., Nguyen, H. T., O'Halloran, B., Omont, A., Page, M. J., Panuzzo, P., Papageorgiou, A., Patel, H., Pearson, C. P., Pérez-Fournon, I., Pohlen, M., Rawlings, J. I., Raymond, G., Rigopoulou, D., Riguccini, L., Rizzo, D., Rodighiero, G., Roseboom, I. G., Rowan-Robinson, M., Sánchez Portal, M., Schulz, B., Scott, D., Seymour, N., Shupe, D. L., Smith, A. J., Stevens, J. A., Symeonidis, M., Trichas, M., Tugwell, K. E., Vaccari, M., Valtchanov, I., Vieira, J. D., Viero, M., Vigroux, L., Wang, L., Ward, R., Wardlow, J., Wright, G., Xu, C. K., and Zemcov, M. (2012). The Herschel Multi-tiered Extragalactic Survey: HerMES. *Monthly Notices of the Royal Astronomical Society*, 424:1614–1635. 14

Pilbratt, G. L., Riedinger, J. R., Passvogel, T., Crone, G., Doyle, D., Gageur, U., Heras, A. M., Jewell, C., Metcalfe, L., Ott, S., and Schmidt, M. (2010). Herschel space observatory*. *A&A*, 518:L1. 6

Poglitsch, A., Waelkens, C., Geis, N., Feuchtgruber, H., Vandenbussche, B., Rodriguez, L., Krause, O., Renotte, E., van Hoof, C., Saraceno, P., Cepa, J., Kerschbaum, F., Agnèse, P., Ali, B., Altieri, B., Andreani, P., Augueres, J.-L., Balog, Z., Barl, L., Bauer, O. H., Belbachir, N., Benedettini, M., Billot, N., Boulade, O., Bischof, H., Blommaert, J., Callut, E., Cara, C., Cerulli, R., Cesarsky, D., Contursi, A., Creten, Y., De Meester, W., Doublier, V., Doumayrou, E., Duband, L., Exter, K., Genzel, R., Gillis, J.-M., Grözinger, U., Henning, T., Herreros, J., Huygen, R., Inguscio, M., Jakob, G., Jamar, C., Jean, C., de Jong, J., Katterloher, R., Kiss, C., Klaas, U., Lemke, D., Lutz, D., Madden, S., Marquet, B., Martignac, J., Mazy, A., Merken, P., Montfort, F., Morbidelli, L., Müller, T., Nielbock, M., Okumura, K., Orfei, R., Ottensamer, R., Pezzuto, S., Popesso, P., Putzeys, J., Regibo, S., Reveret, V., Royer, P., Sauvage, M., Schreiber, J., Stegmaier, J., Schmitt, D., Schubert, J., Sturm, E., Thiel, M., Tofani, G., Vavrek, R., Wetzstein, M., Wieprecht, E., and Wiezorrek, E. (2010). The Photodetector Array Camera and Spectrometer (PACS) on the Herschel Space Observatory. *Astronomy and Astrophysics*, 518:L2. 7

Polletta, M., Tajer, M., Maraschi, L., Lonsdale, C. J., Chiappetti, L., Andreon, S., Pierre, M.,

Le Fevre, O., Zamorani, Z., Maccagni, D., Garcet, O., Surdej, J., Franceschini, A., Alloin, D. ad Shupe, D. L., Surace, J. A., Fang, F., Rowan-Robinson, M., Smith, H. E., and Tresse, L. (2007). Spectral Energy Distributions of Hard X-Ray Selected Active Galactic Nuclei in the XMM-Newton Medium Deep Survey. *The Astrophysical Journal*, 663:81. 8, 38

Postman, M. and Geller, M. J. (1984). The Morphology-Density Relation. *The Astrophysical Journal*, 281:95. 3

Ptak, A., Heckman, T., Levenson, N. A., Weaver, K., and Strikland, D. (2003). A Chandra Survey of the Nearest Ultraluminous Infrared Galaxies: Obscured Active Galactic Nuclei or Superstarbursts? *The Astrophysical Journal*, 592:782–803. 11

Rieke, G. H. (1988). Hard X-ray observations of ultraluminous infrared galaxies. *The Astrophysical Journal Letters*, 331:L5–L8. 11

Rieke, G. H. and Low, F. J. (1972). Infrared Photometry of Extragalactic Sources. *The Astrophysical Journal*, 176:L95. 11

Rieke, G. H., Young, E. T., Engelbracht, C. W., Kelly, D. M., Low, F. J., Haller, E. E., Beeman, J. W., Gordon, K. D., Stansberry, J. A., Misselt, K. A., Cadien, J., Morrison, J. E., Rivlis, G., Latter, W. B., Noriega-Crespo, A., Padgett, D. L., Stapelfeldt, K. R., Hines, D. C., Egami, E., Muzerolle, J., Alonso-Herrero, A., Blaylock, M., Dole, H., Hinz, J. L., Le Floc'h, E., Papovich, C., Pérez-González, P. G., Smith, P. S., Su, K. Y. L., Bennett, L., Frayer, D. T., Henderson, D., Lu, N., Masci, F., Pesenson, M., Rebull, L., Rho, J., Keene, J., Stolovy, S., Wachter, S., Wheaton, W., Werner, M. W., and Richards, P. L. (2004). The Multiband Imaging Photometer for Spitzer (MIPS). *The Astrophysical Journal Supplement Series*, 154:25–29. 6

Rigopoulou, D., Genzel, R., Lutz, D., Spoon, H., Sturm, E., Kunze, D., Tran, D., and Moorwood, A. (1996). A low resolution spectroscopic survey of Ultraluminous Infrared Galaxies. *Astronomische Gesellschaft Meeting Abstracts*. 13

Rigopoulou, D., Lawrence, A., and Rowan-Robinson, M. (1998). Multiwavelength energy distributions of ultraluminous IRAS galaxies - I. Submillimetre and X-ray observations. *Monthly Notices of the Royal Astronomical Society*, 278:1049–1068. 13

Rowan-Robinson, M., Clegg, P., Beichman, C. A., Neugebauer, G., Soifer, B. T., Aumann, H. H., Beintema, D. A., Boggess, N., Emerson, J. P., Gautier, T. N., Gillett, F. C., Hauser, M. G., Houck, J. R., Low, F. J., and Walker, R. G. (1984). The IRAS Minisurvey. *The Astrophysical Journal*, 278:L7–L10. 11

Sanders, D. B. and Mirabel, I. F. (1996). Luminous Infrared Galaxies. *Annual Review of Astronomy and Astrophysics*, 34:749. 11

Saslaw, W. C. (1987). *Gravitational Physics of Stellar and Galactic Systems*. Cambridge University Press. 3

Smith, J. (2007). The Mid-Infrared Spectrum of Star-Forming Galaxies: Global Properties of Polycyclic Aromatic Hydrocarbons. *The Astrophysical Journal*, 656:770. 9

Soifer, B., Sanders, D., Madore, B., Neugebauer, G., Danielson, G., Elias, J., Lonsdale, C. J., and Rice, W. (1987). The iras bright galaxy sample. ii-the sample and luminosity function. *The Astrophysical Journal*, 320:238–257. 11

Soifer, B. T., Rowan-Robinson, M., Houck, J. R., de Jong, T. Neugebauer, G., Aumann, H. H., Beichman, C. A., Boggess, N., Clegg, P. E. Emerson, J. P., Gillett, F. C., Habing, H. J., Hauser, M. G., Low, F. J., Miley, G., and Young, E. (1984). Infrared Galaxies in the IRAS minisurvey. *The Astrophysical Journal*, 278:L71–L74. 11

van den Bergh, S. (1960). A Preliminary Luminosity Classification of Late-Type Galaxies. *The Astrophysical Journal*, 131:215. 1

Werner, M. W., Roellig, T. L., Low, F. J., Rieke, G. H., Rieke, M., Hoffmann, W. F., Young, E., Houck, J. R., Brandl, B., Fazio, G. G., Hora, J. L., Gehrz, R. D., Helou, G., Soifer, B. T., Stauffer, J., Keene, J., Eisenhardt, P., Gallagher, D., Gautier, T. N., Irace, W., Lawrence, C. R., Simmons, L., Van Cleve, J. E., Jura, M., Wright, E. L., and Cruikshank, D. P. (2004). The Spitzer Space Telescope Mission. *The Astrophysical Journal Supplement Series*, 154:1–9. 6

Appendix A

Source Lists

On this page and the next, the positions, IRAC fluxes and MIPS-24 fluxes of the first hundred ULIRGs in the Lockman-SWIRE field are listed in Table A. This sample is tabulated here in order to provide an illustration of the properties of the galaxies chosen. The complete listing will be made available online.

Values which show as -9.9 means that there is not a flux estimate at that wavelength, either because the sky area was not observed (or was masked) or because the sky area was observed but the source not detected. As we are restricted to areas covered by all of the four IRAC channels and MIPS-24μm, then a value of -9.9 will indicate that the source is below the flux limit in the given band, which can be estimated on the basis of where the source counts start to fall off.

RA	Dec	r-band magnitude	3.6μm flux density (μJy)	4.5μm flux density (μJy)	5.8μm flux density (μJy)	8.0μm flux density (μJy)	24μm flux density (mJy)
158.015305	58.131069	-9.900000	54.220001	56.099998	-9.900000	55.360001	456.959991
158.021439	57.804909	-9.900000	68.220001	86.529999	73.580002	75.269997	698.729980
158.380432	58.328876	22.433201	141.100006	144.789993	135.880005	113.290001	500.320007
158.389145	57.853779	-9.900000	52.959999	54.040001	46.570000	-9.900000	465.779999
158.393433	58.261398	-9.900000	37.340000	51.450001	-9.900000	-9.900000	749.330017
158.438095	57.942619	24.259001	52.630001	58.230000	39.310001	52.590000	489.690002
158.453751	57.742649	23.562000	55.750000	62.180000	56.169998	57.779999	441.019989
158.460785	58.237377	-9.900000	58.049999	65.330002	-9.900000	-9.900000	468.070007
158.475662	58.474537	-9.900000	33.470001	43.250000	-9.900000	-9.900000	385.709991
158.491974	58.062897	-9.900000	82.129997	85.300003	58.520000	76.860001	527.369995
158.495010	57.660000	22.791901	71.599998	79.959999	58.540001	76.669998	521.690002
158.619568	58.636806	-9.900000	55.500000	60.049999	52.599998	-9.900000	543.309998
158.647079	58.523350	-9.900000	75.870003	84.699997	54.060001	69.160004	445.369995
158.647614	58.147469	-9.900000	34.419998	43.330002	37.180000	-9.900000	350.450012
158.778320	58.698540	-9.900000	52.020000	68.050003	63.720001	-9.900000	450.079987
158.825455	57.844349	23.787001	92.980003	119.870003	99.449997	74.949997	450.679993
158.839218	58.664330	23.582001	44.869999	52.189999	-9.900000	-9.900000	489.809998
158.842651	58.658417	23.643999	73.290001	73.930000	62.470001	60.669998	438.850006
158.865967	57.801189	-9.900000	31.799999	44.310001	41.259998	-9.900000	401.049988
158.870056	58.303570	24.170000	56.220001	58.520000	48.610001	-9.900000	450.559998
158.899551	57.605698	24.006001	43.340000	49.310001	42.570000	-9.900000	398.630005
158.928024	58.188869	-9.900000	74.540001	89.650002	-9.900000	-9.900000	447.179993
158.949478	57.496029	-9.900000	39.720001	48.820000	48.259998	-9.900000	548.020020
158.989395	58.394867	23.631001	102.510002	109.440002	87.160004	79.279999	640.760010
159.004745	58.757847	23.540001	44.209999	50.430000	38.689999	47.910000	470.130005
159.025864	57.922577	23.443001	34.419998	44.599998	32.000000	-9.900000	376.170013
159.032974	57.392807	24.268999	76.910004	85.459999	67.610001	73.940002	363.730011
159.043945	58.710327	22.739000	110.150002	120.559998	84.379997	77.570000	461.790009
159.046356	57.380039	23.775999	40.580002	51.660000	-9.900000	-9.900000	511.670013
159.062408	57.918240	23.143000	80.769997	100.070000	78.379997	53.939999	512.390015
159.077927	58.767109	23.716999	39.080002	52.689999	51.619999	41.810001	743.409973
159.088913	59.109627	-9.900000	49.869999	50.000000	-9.900000	-9.900000	373.880005
159.102432	57.540787	23.596001	42.779999	50.150002	-9.900000	-9.900000	413.970001
159.104752	57.997219	23.320000	32.820000	43.540001	36.919998	-9.900000	426.890015
159.118317	58.001717	23.615999	41.869999	51.700001	42.590000	-9.900000	377.260010
159.137939	59.193520	-9.900000	41.330002	51.130001	-9.900000	-9.900000	442.589996
159.142014	57.902180	-9.900000	35.889999	46.439999	45.090000	-9.900000	425.809998
159.151688	59.224979	-9.900000	36.610001	52.669998	37.709999	-9.900000	425.809998
159.159714	58.198418	23.605000	83.160004	84.029999	59.910000	66.699997	466.989990
159.178894	57.991859	24.129999	54.000000	62.560001	61.759998	51.380001	367.119995
159.195511	59.245560	-9.900000	37.360001	49.509998	-9.900000	40.500000	479.540009
159.199585	57.919617	-9.900000	33.590000	43.700001	-9.900000	-9.900000	450.799988
159.220047	58.312057	-9.900000	40.290001	47.270000	41.669998	-9.900000	676.390015
159.240494	58.687576	-9.900000	39.080002	50.119999	38.180000	-9.900000	611.169983
159.255768	59.139389	-9.900000	48.799999	59.830002	48.320000	-9.900000	407.209991
159.267197	59.265610	-9.900000	46.619999	53.549999	53.020000	-9.900000	355.279999
159.268234	57.933697	23.263000	43.349998	51.400002	44.220001	39.029999	433.529999
159.287354	59.217190	-9.900000	63.750000	76.930000	71.459999	51.880001	457.929993
159.291061	58.093777	22.677000	70.239998	78.610001	64.410004	54.180000	510.820007
159.291672	59.266468	-9.900000	43.480000	54.880001	52.849998	49.060001	384.989990
159.332275	59.006428	-9.900000	47.520000	56.669998	45.860001	-9.900000	629.890015

RA	Dec	r-band magnitude	3.6μm flux density (μJy)	4.5μm flux density (μJy)	5.8μm flux density (μJy)	8.0μm flux density (μJy)	24μm flux density (mJy)
159.354492	57.963577	-9.900000	34.660000	49.209999	-9.900000	49.000000	845.330017
159.368057	58.643669	-9.900000	44.490002	61.919998	60.799999	58.650002	581.469971
159.386108	57.810650	23.306000	62.689999	63.779999	38.099998	56.910000	367.839996
159.404785	57.817539	24.427000	85.680000	86.730003	48.110001	72.129997	412.880005
159.421707	58.541039	-9.900000	50.750000	68.739998	64.870003	37.820000	463.119995
159.427078	57.495209	22.120199	35.349998	44.730000	-9.900000	-9.900000	495.000000
159.439224	58.059368	-9.900000	40.220001	45.970001	34.099998	-9.900000	491.619995
159.444458	57.897499	23.263000	35.630001	45.259998	-9.900000	-9.900000	756.450012
159.479431	57.996326	-9.900000	59.400002	64.910004	43.480000	46.279999	438.119995
159.495758	59.326847	-9.900000	37.619999	48.750000	-9.900000	-9.900000	610.929993
159.533905	58.288269	-9.900000	44.200001	55.279999	54.060001	45.340000	511.670013
159.541443	57.564507	23.823000	68.970001	80.150002	44.810001	45.959999	485.700012
159.553665	58.349289	23.688999	44.099998	50.750000	34.090000	43.820000	404.670013
159.577805	58.238918	-9.900000	59.770000	72.059998	-9.900000	-9.900000	664.909973
159.606522	58.886238	-9.900000	53.070000	53.930000	45.930000	-9.900000	499.950012
159.621017	57.926968	22.096001	72.620003	84.910004	56.230000	-9.900000	526.159973
159.627655	59.171619	-9.900000	72.900002	82.540001	61.650002	54.299999	357.820007
159.663208	58.986649	-9.900000	85.760002	99.550003	92.949997	77.129997	436.190002
159.683121	58.939850	23.521000	67.849998	82.239998	74.940002	-9.900000	632.309998
159.692505	58.231979	-9.900000	42.580002	50.740002	34.689999	-9.900000	366.630005
159.694702	58.756268	-9.900000	43.080002	46.950001	-9.900000	-9.900000	355.399994
159.727173	58.204659	-9.900000	55.790001	69.019997	60.570000	-9.900000	352.140015
159.758224	58.428497	23.618999	86.949997	93.089996	60.950001	56.380001	431.000000
159.767365	57.917427	24.382999	51.889999	60.500000	57.790001	38.380001	369.649994
159.769424	58.531498	-9.900000	39.480000	43.090000	37.669998	-9.900000	421.940002
159.785889	58.562828	-9.900000	43.090000	52.720001	-9.900000	-9.900000	402.739990
159.792343	58.348976	-9.900000	37.389999	44.740002	37.410000	-9.900000	457.079987
159.806793	58.243919	22.686001	43.410000	53.500000	47.240002	-9.900000	437.760010
159.823441	59.241940	-9.900000	34.049999	43.480000	41.830002	-9.900000	679.650024
159.832993	57.659599	22.910000	81.889999	83.610001	-9.900000	69.059998	779.520020
159.849884	57.020416	-9.900000	35.419998	44.360001	-9.900000	-9.900000	359.869995
159.863235	57.648930	-9.900000	47.340000	59.369999	-9.900000	52.730000	738.940002
159.871506	59.205349	23.252001	46.099998	50.900002	48.889999	-9.900000	602.840027
159.883560	58.426247	23.466999	34.680000	43.270000	-9.900000	-9.900000	509.489990
159.938766	58.076778	-9.900000	45.160000	51.750000	40.529999	-9.900000	355.040009
159.944977	59.287457	-9.900000	43.380001	49.740002	34.070000	37.580002	380.519989
159.955811	58.943890	22.781000	54.110001	55.130001	-9.900000	49.990002	442.230011
159.961121	59.698708	-9.900000	39.320000	51.320000	-9.900000	-9.900000	432.690002
159.967285	57.662060	-9.900000	32.849998	43.270000	-9.900000	36.599998	465.290009
159.972382	57.021267	22.068300	38.259998	44.590000	-9.900000	-9.900000	366.269989
159.979736	58.494370	-9.900000	45.020000	53.220001	33.230000	-9.900000	432.929993
160.011337	59.542728	-9.900000	52.040001	52.220001	46.180000	-9.900000	495.000000
160.019485	56.948460	23.313999	37.310001	45.580002	-9.900000	-9.900000	880.840027
160.024323	58.520996	23.101299	49.380001	50.669998	42.389999	-9.900000	390.660004
160.026611	58.776150	-9.900000	43.939999	51.950001	41.660000	39.540001	751.500000
160.029083	57.330589	23.486000	52.169998	64.010002	-9.900000	-9.900000	409.019989
160.048248	58.095287	-9.900000	63.549999	76.730003	64.839996	-9.900000	750.900024
160.052368	58.566437	23.077999	76.690002	78.089996	52.790001	-9.900000	453.100006
160.075974	57.722630	-9.900000	41.209999	49.820000	-9.900000	-9.900000	545.960022

Table A.1: Positions, IRAC flux densities and MIPS 24μm flux densities for the first hundred ULIRGs in the Lockman-IRAC field sample.

Appendix B

Source Images

A selection of postage stamp images of the ULIRGs are presented on the following pages as examples of the objects sampled in this study. These are shown for the first hundred sources from the Lockman-SWIRE field in Figure B, and each object is shown at five different wavelengths in the near- and mid-infrared. The full set of images will be made available online. From left to right the object is shown in the four IRAC bands of 3.6μm, 4.5μm, 5.8μm and 8.0μm, followed by the MIPS 24μm image.

The size of these postage stamps are 21 x 21 pixels, and the pixel size at 250μm is 6"/pixel, so the images are 21 $\times$ 6 = 126" across. The angular scale at redshift 1.7 is 8.555 kpc/", hence this angular size corresponds to a distance of 8.555 $\times$ 126 = 1078 kpc. The stamps therefore illustrate a $\sim$ 1 Mpc region around the objects of interest.

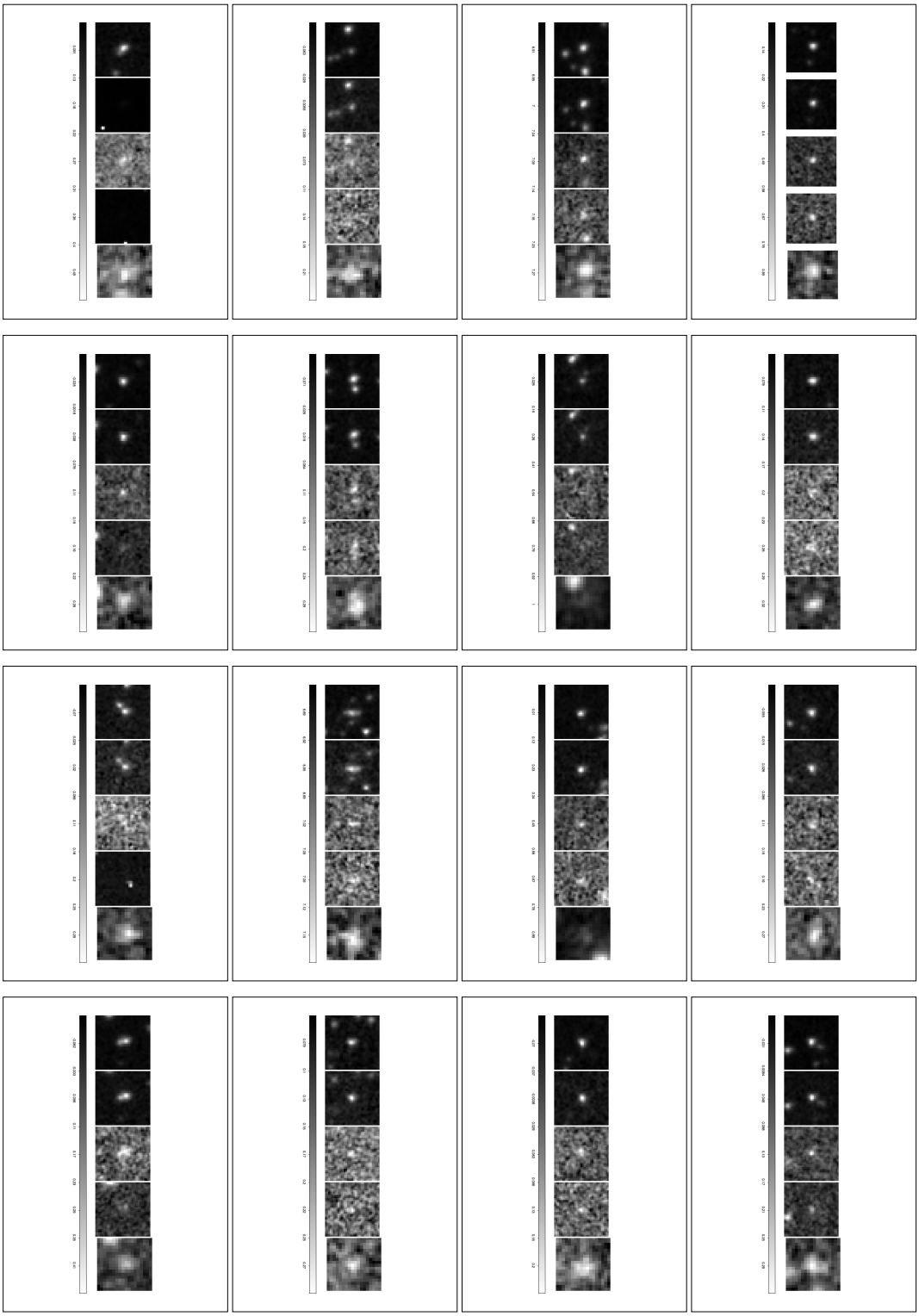

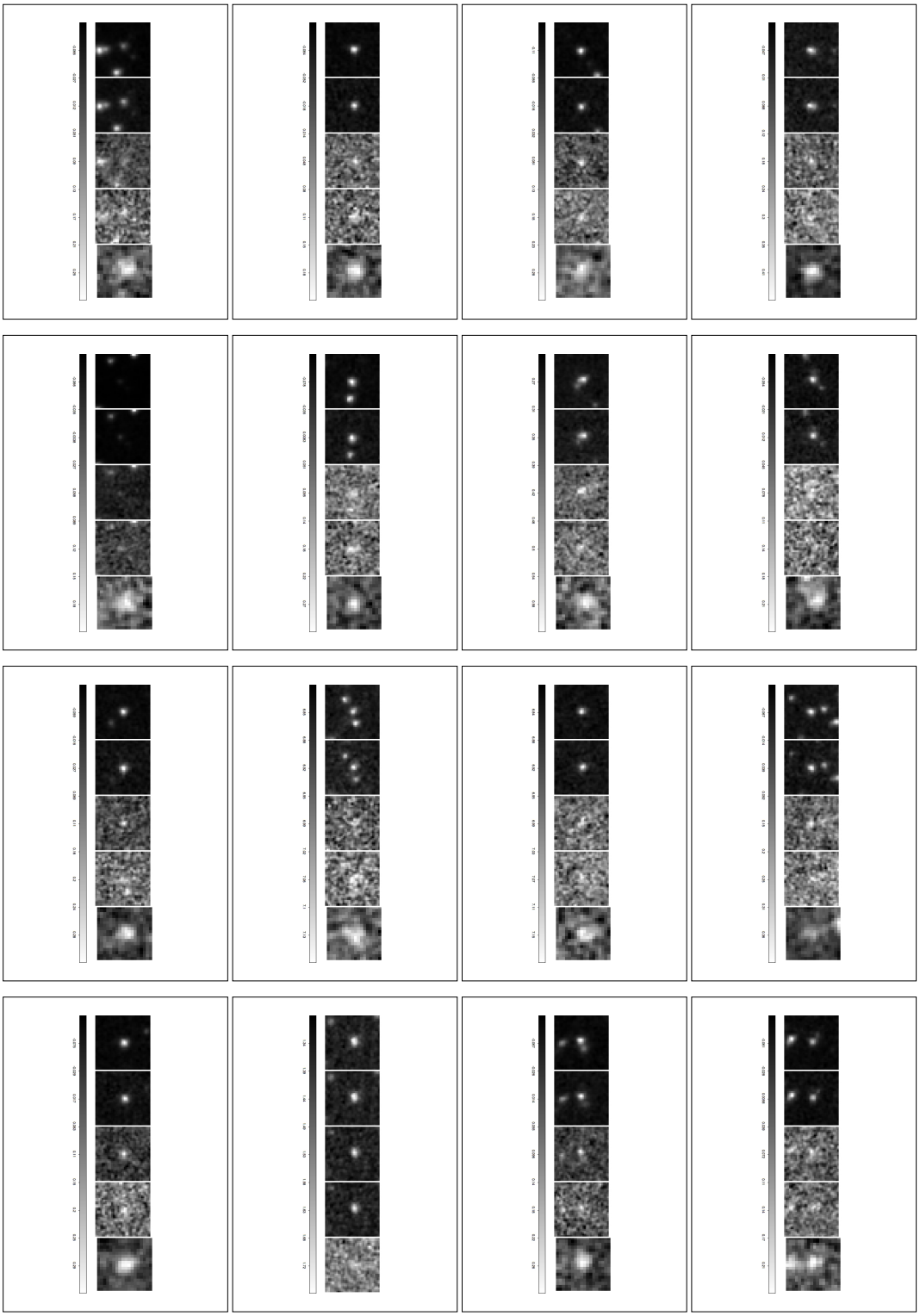

s

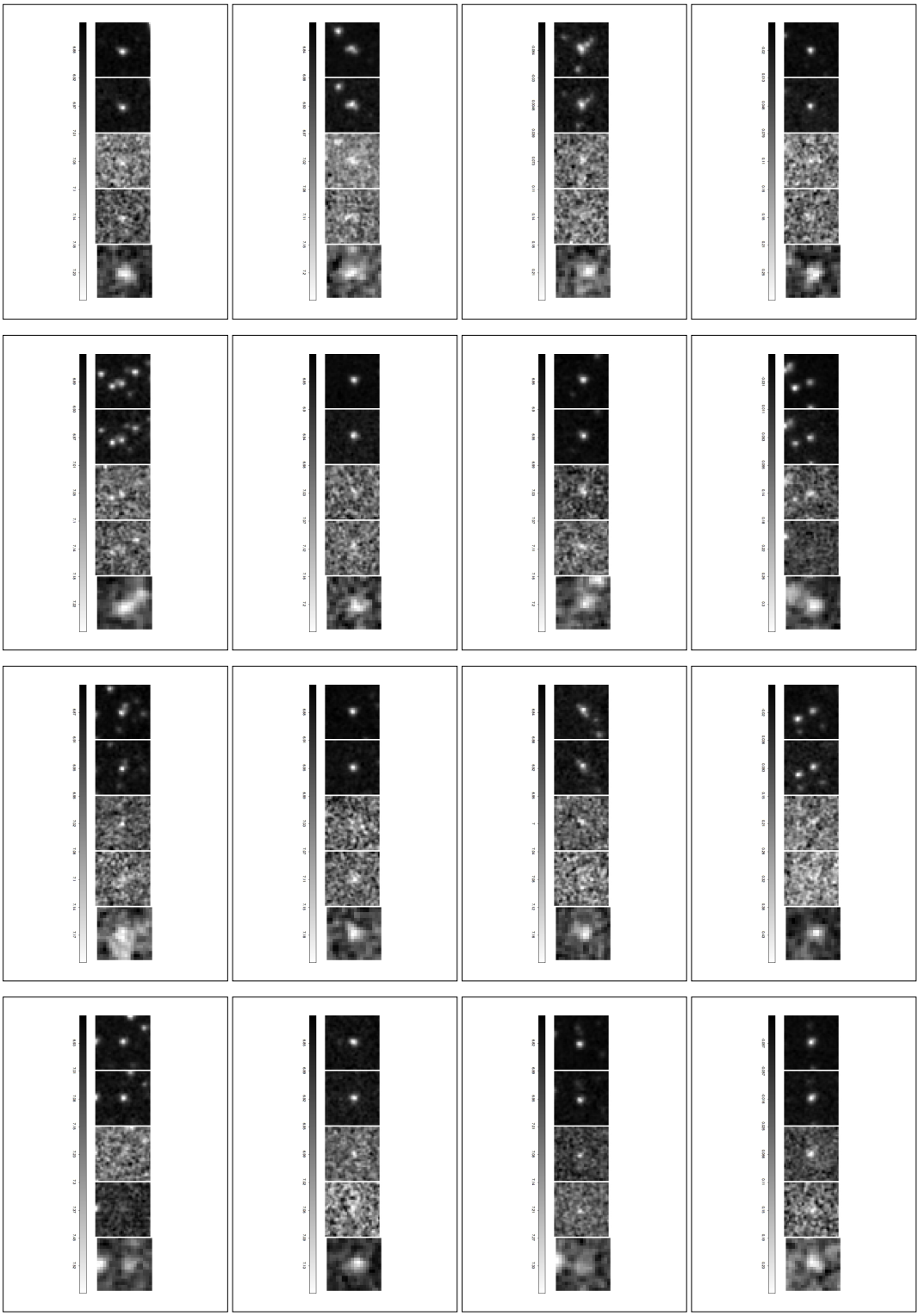

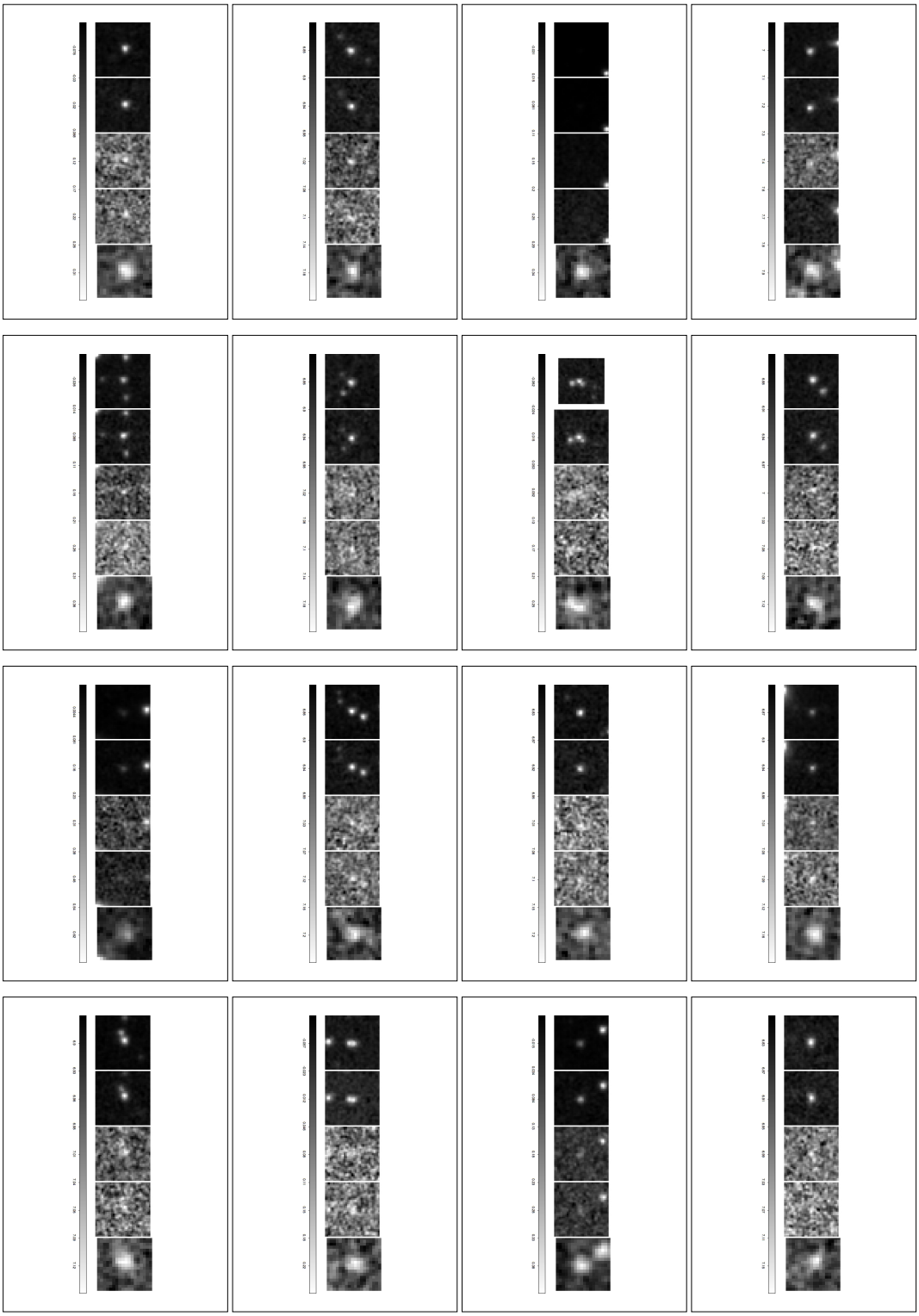

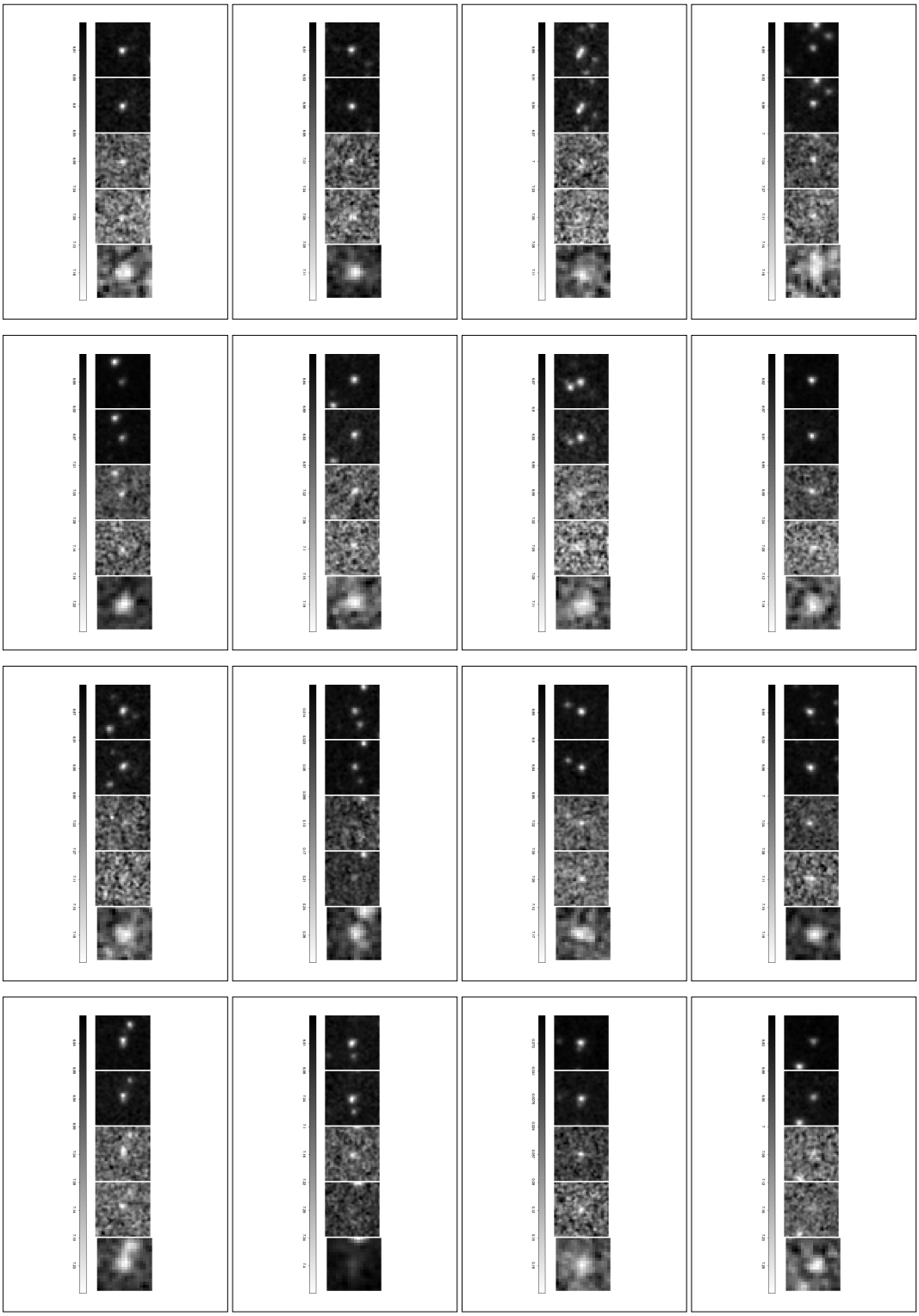

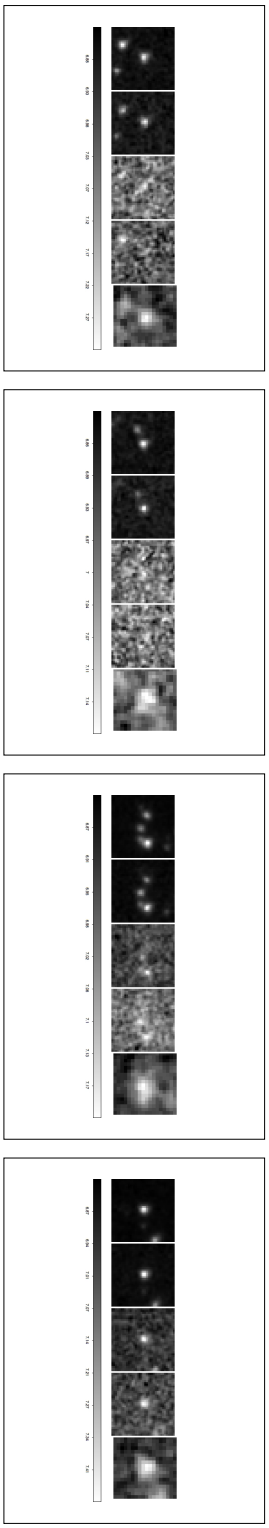

Figure B.1: Postage stamp images at IRAC and 24 μm wavelengths for the first hundred ULIRGs in the Lockman-IRAC field sample.